

Nitrogen as a Tracer of Giant Planet Formation. II.: Comprehensive Study of Nitrogen Photochemistry and Implications for Observing NH₃ and HCN in Transmission and Emission Spectra

KAZUMASA OHNO^{1,2} AND JONATHAN J. FORTNEY²

¹*Division of Science, National Astronomical Observatory of Japan, 2-21-1 Osawa, Mitaka-shi, Tokyo, Japan*

²*Department of Astronomy & Astrophysics, University of California, Santa Cruz, 1156 High St, Santa Cruz, CA 95064, USA*

ABSTRACT

Atmospheric nitrogen may provide important constraints on giant planet formation. Following our semi-analytical work (Ohno & Fortney 2023), we further pursue the relation between observable NH₃ and an atmosphere's bulk nitrogen abundance by applying the photochemical kinetics model VULCAN across planetary equilibrium temperature, mass, age, eddy diffusion coefficient, atmospheric composition, and stellar spectral type. We confirm that the quenched NH₃ abundance coincides with the bulk nitrogen abundance only at sub-Jupiter mass ($\lesssim 1M_J$) planets and old ages ($\gtrsim 1$ Gyr) for solar composition atmospheres, highlighting important caveats for inferring atmospheric nitrogen abundances. Our semi-analytical model reproduces the quenched NH₃ abundance computed by VULCAN and thus helps to infer the bulk nitrogen abundance from a retrieved NH₃ abundance. By computing transmission and emission spectra, we predict that the equilibrium temperature range of 400–1000 K is optimal for detecting NH₃ because NH₃ depletion by thermochemistry and photochemistry is significant at hotter planets whereas entire spectral features become weak at colder planets. For Jupiter-mass planets around Sun-like stars in this temperature range, NH₃ leaves observable signatures of ~ 50 ppm at 1.5, 2.1, and 11 μm in transmission spectra and > 300 –100 ppm at 6 μm and 11 μm in emission spectra. The photodissociation of NH₃ leads HCN to replace NH₃ at low pressures. However, the low HCN column densities lead to much weaker absorption features than for NH₃. The NH₃ features are readily accessible to JWST observations to constrain atmospheric nitrogen abundances, which may open a new avenue to understand the formation processes of giant exoplanets.

1. INTRODUCTION

The composition of giant planet atmospheres offer valuable clues to the planet formation process. Over the past decade a number of studies have suggested that atmospheric elemental ratios, such as the carbon-to-oxygen ratio (C/O), can diagnose a giant planet's formation location and accretion history within a disk (e.g., Öberg et al. 2011; Öberg & Bergin 2016; Öberg & Wordsworth 2019; Madhusudhan et al. 2014, 2017; Ali-Dib et al. 2014; Helling et al. 2014; Thiabaud et al. 2015; Piso et al. 2015, 2016; Espinoza et al. 2017; Eistrup et al. 2016, 2018, 2022; Cridland et al. 2016, 2017, 2019; Booth et al. 2017; Booth & Ilee 2019; Ohno & Ueda 2021; Turrini et al. 2021; Schneider & Bitsch 2021a; Mollière et al. 2022; Pacetti et al. 2022; Bitsch et al. 2022; Eistrup 2022). Recent studies also suggest that nitrogen provides valuable insights on the planet formation processes (Piso et al. 2016; Cridland et al. 2020; Ohno & Ueda 2021; Turrini et al. 2021; Notsu et al. 2022). Several studies have discussed the formation environment of Jupiter in our Solar System based on atmospheric nitrogen and noble gas abundances (e.g., Owen et al. 1999; Gautier et al. 2001; Guillot & Hueso 2006; Monga & Desch 2015; Ali-Dib 2017; Mousis

et al. 2019; Öberg & Wordsworth 2019; Bosman et al. 2019; Ohno & Ueda 2021; Aguichine et al. 2022).

NH₃ and HCN are likely the most easily accessible nitrogen species in giant exoplanet atmospheres via spectroscopy (MacDonald & Madhusudhan 2017a), as the remaining main nitrogen reservoir N₂ has negligibly low visible and infrared opacity. However, constraining an atmosphere's bulk nitrogen abundance from NH₃ and HCN is a complex task. It is well known from previous work that the NH₃ and HCN abundances in the observable atmosphere readily deviates from thermochemical equilibrium abundances due to vertical mixing and photochemistry (e.g., Moses et al. 2011; Line et al. 2011; Venot et al. 2013). For warm planets with $T_{\text{eq}} \lesssim 1200$ K, Fortney et al. (2020) investigated disequilibrium NH₃ abundances on Saturn-like planets across T_{eq} -space and found that the NH₃ abundance depends on a number of factors, such as planetary mass, age, and metallicity. Ohno & Fortney (2023) (hereafter Paper I) further generalized the conditions under which the vertically quenched NH₃ abundance coincides with the bulk nitrogen abundance, based on a suite of radiative-convective atmosphere models and semi-analytical arguments. Paper I suggested that the NH₃ abundance coincides with the bulk nitrogen abundance only at sub-Jupiter planetary mass ($\lesssim 1M_{\text{Jup}}$), old age ($\gtrsim 1$

Gyr), and low atmospheric metallicity ($< 10\times$ solar value); otherwise, N_2 dominates over NH_3 , making the observable NH_3 abundance only a lower limit of bulk nitrogen abundance.

Fortney et al. (2020) and Paper I relied on the so-called quench approximation that estimates the vertically quenched NH_3 abundance from timescale arguments; however, the quench approximation is not always accurate. While the quench approximation yields vertically-constant abundance of disequilibrium species, Tsai et al. (2018) showed that the abundance can vary with altitudes even above the quench pressure level, especially for hot atmospheres. Molaverdikhani et al. (2019) also pointed that molecular diffusion and photodissociation can cause vertically nonuniform abundance profiles. In fact, Hu (2021) investigated photochemistry on template/cold H_2 -rich planets and found that NH_3 tends to be readily depleted due to photodissociation, especially on planets around G/K stars. Thus, it is essential to use a detailed photochemical kinetics model to establish a comprehensive understanding on the relation between observable NH_3 and bulk nitrogen abundance.

In this paper, we continue exploring the relation between observable nitrogen species and bulk nitrogen abundances—the total nitrogen abundance in the atmosphere—using a photochemical kinetics model. The organization of this paper is as follows. In Section 2, we briefly review the semi-analytical relationship of disequilibrium NH_3 and bulk nitrogen abundances predicted by Paper I. In Section 3, we apply a photochemical kinetics model to a wide range of planetary parameters to comprehensively understand the relation between observable NH_3 and bulk nitrogen abundance. In Section 4, we investigate the observational feasibility of detecting nitrogen species in transmission and emission spectra. In Section 5, we discuss the effects of stellar spectral type, the presence of photochemical hazes, and day-night temperature contrast. In Section 6, we summarize our findings.

2. SEMI-ANALYTICAL RELATION BETWEEN NH_3 AND BULK NITROGEN ABUNDANCES

In Paper I, based on the the law of mass action and a semi-analytic pressure-temperature (P-T) profile for deep adiabatic atmosphere, we established a semi-analytical model that predicts the vertically quenched NH_3 abundance of warm giant planets with $T_{eq} \sim 250\text{--}1200$ K as a function of the bulk nitrogen abundance. This is given by

$$\frac{f_{NH_3}}{f_N} = \frac{\sqrt{1 + 8\mathcal{K}^{-1}} - 1}{4}\mathcal{K}, \quad (1)$$

where f_{NH_3} is the volume mixing ratio of the quenched NH_3 , f_N is the bulk nitrogen abundance, and \mathcal{K} is the dimensionless parameter given by

$$\mathcal{K} \approx 3.46 \times 10^{-0.8[Fe/H]} \left(\frac{f_N}{10^{-4}} \right)^{-1} \left(\frac{g}{10 \text{ m s}^{-2}} \right)^{4/3} \left(\frac{T_{int}}{100 \text{ K}} \right)^{-16/3} \quad (2)$$

where $[Fe/H]$ is the atmospheric metallicity, g is the surface gravity, and T_{int} is the planetary intrinsic temperature. The bulk nitrogen abundance f_N is associated to nitrogen-to-hydrogen ratio N/H as

$$f_N = \frac{N}{H_2 + He} = 2f_{H_2}N/H, \quad (3)$$

where $f_{H_2} = H_2/(H_2 + He) = 0.859$ and $f_N = 1.16 \times 10^{-4}$ in the solar elemental abundances of Asplund et al. (2021). Paper I also provides an alternative form of Equation (1), which can be used to infer the bulk nitrogen abundance from a retrieved NH_3 abundance, as

$$\frac{f_N}{f_{NH_3}} \approx 1 + 0.58 \times 10^{0.8[Fe/H]} \left(\frac{f_{NH_3}}{10^{-4}} \right) \left(\frac{g}{10 \text{ m s}^{-2}} \right)^{-4/3} \left(\frac{T_{int}}{100 \text{ K}} \right)^{16/3} \quad (4)$$

This theory assumes that the quenched NH_3 abundance is insensitive to planetary equilibrium temperature and eddy diffusion coefficient. This seemingly extreme assumption is valid because warm giant exoplanets have nearly the same deep atmosphere adiabatic profile at a given intrinsic flux and gravity (Fortney et al. 2007, 2020; Paper I) and the thermochemical equilibrium abundance of NH_3 is nearly constant along the deep adiabat for a given bulk nitrogen abundance (Saumon et al. 2006; Zahnle & Marley 2014; Fortney et al. 2020).

Equation (1) tells us how the quenched NH_3 abundance relates with the bulk nitrogen abundance. For example, the NH_3 abundance is nearly the same as bulk nitrogen abundance, i.e., $f_{NH_3} \approx f_N$, at $\mathcal{K} \gg 8$. By contrast, in the limit of low \mathcal{K} , the NH_3 abundance obeys $f_{NH_3} \approx f_N \sqrt{\mathcal{K}/2}$ that is lower than the bulk nitrogen abundance because of the conversion from NH_3 to N_2 . It is worth noting that the semi-analytic theory predicts that the quenched NH_3 abundance is insensitive to the metallicity in the N_2 rich regime (low \mathcal{K} limit). When the bulk nitrogen abundance is scaled by the atmospheric metallicity, i.e., $f_N \propto 10^{[Fe/H]}$, Equation (1) yields the nearly metallicity-independent NH_3 abundance of $f_{NH_3} \propto 10^{0.1[Fe/H]}$. This insensitivity is owing to combined effects of hot deep interiors in the high metallicity atmospheres, and the preference for N_2 over NH_3 at higher metallicity (Lodders & Fegley 2002; Moses et al. 2013b).

Since the quenched NH_3 abundance depends only on g and T_{int} for given metallicity, we can predict the quenched NH_3 abundance as a function of planetary mass and age, which control g and T_{int} . Figure 1 shows the predicted quenched NH_3 abundance at various planetary masses and ages, taken from Paper I. The quenched NH_3 abundance is higher at lower planetary mass and older age because of the cool deep atmosphere for these planets. We predicted that, for solar composition atmospheres, the quenched NH_3 diagnoses more than 50% of bulk nitrogen only when the planet has a sub-Jupiter mass ($\lesssim 1M_J$) and old age ($\gtrsim 1$ Gyr). The

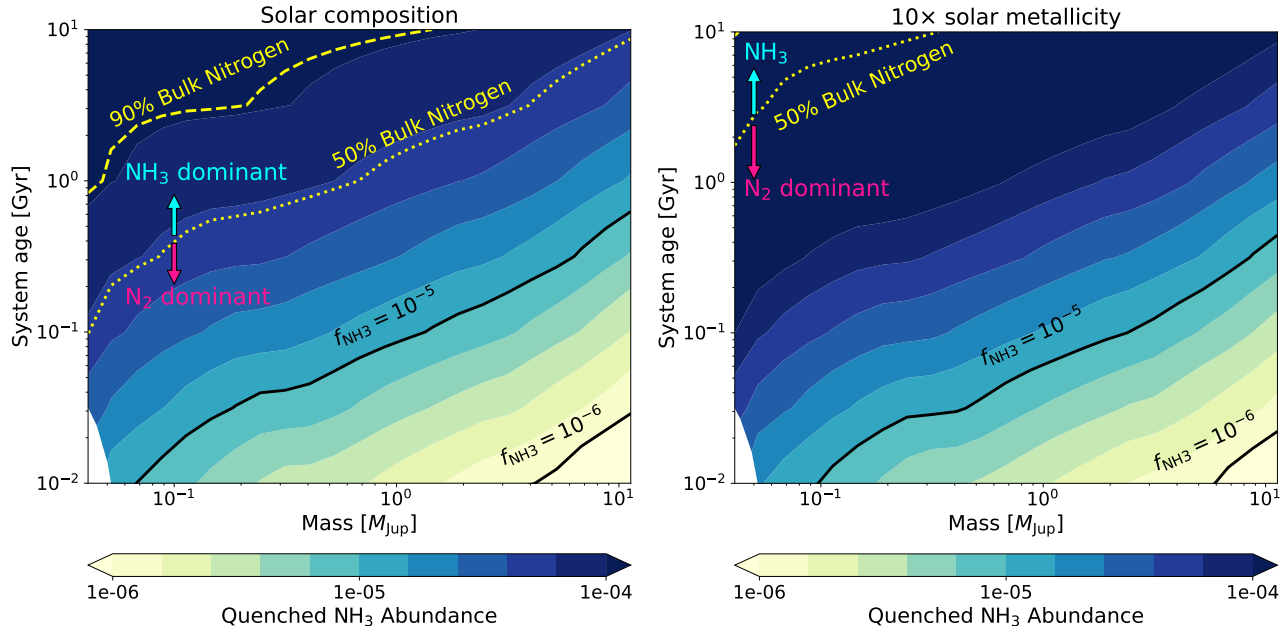


Figure 1. The quenched NH_3 abundance predicted by the semi-analytic model of Paper I (Equation 1) as a function of planetary mass and age, where g and T_{int} are extracted from the thermal evolution tracks of Fortney et al. (2007). The black line denotes the abundance contours of $f_{\text{NH}_3} = 10^{-5}$ and 10^{-6} , and yellow dashed and dotted lines show the contours corresponding to 90% and 50% of the bulk nitrogen abundance. The left and right columns show the results for solar metallicity and $10\times$ solar metallicity atmosphere, respectively, where we have assumed that the N/H ratio is scaled by the metallicity.

discrepancy becomes even worse at high metallicity (for instance ≥ 10 solar) atmospheres, for which the quenched NH_3 abundance is significantly lower than the bulk nitrogen abundance at almost all values of planetary mass and age. This analysis suggests the necessity of including a chemical model to properly infer the bulk nitrogen abundance from a retrieved NH_3 abundance, and the observable NH_3 abundance should be regarded as a lower limit of bulk nitrogen abundance in most cases.

The analysis of Paper I is based on a simple analytical argument. In reality, thermochemistry and photochemistry can further alter the vertical distribution of NH_3 abundance. In the next section, we use a photochemical kinetics model to better understand the relationship between observable NH_3 and the bulk nitrogen abundances.

3. COMPREHENSIVE INVESTIGATIONS OF NITROGEN PHOTOCHEMISTRY

3.1. Numerical method

Here, we numerically investigate atmospheric chemical compositions using a publicly available photochemical kinetics code, VULCAN (Tsai et al. 2017, 2021b). The code computes the steady state vertical distributions of chemical compositions by solving the transport equations given by

$$\frac{\partial n_i}{\partial t} = \mathcal{P}_i - \mathcal{L}_i - \frac{\partial \Phi_i}{\partial z}, \quad (5)$$

Table 1. A grid of a part of thermal evolution tracks of giant planets with a core mass of $10M_{\oplus}$ in Fortney et al. (2007), for which we apply VULCAN.

Mass [M_J]	Radius [R_J]	Age [Gyr]	Gravity [m s^{-2}]	T_{int} [K]
0.11	1.14	0.1	2.15	120.4
0.11	0.89	1	3.47	73.9
0.11	0.78	10	4.60	39.0
1.00	1.21	0.1	16.90	287.4
1.00	1.11	1	19.96	157.3
1.00	1.04	10	22.71	83.7

where z is the altitude, n_i is the number density of species i , \mathcal{P}_i and \mathcal{L}_i are their production and loss rates, and ϕ_i is the vertical flux due to eddy and molecular diffusion. While several theoretical studies investigated the eddy diffusion coefficient K_{zz} on exoplanets using global circulation models (Parmentier et al. 2013; Charnay et al. 2015; Zhang & Showman 2018a,b; Menou 2019; Komacek et al. 2019; Menou 2021; Tan 2022), it remains poorly constrained from observations (see Kawashima & Min 2021). Thus, we test a broad range of eddy diffusion coefficient, $K_{zz} = 10^5, 10^8$, and $10^{11} \text{ cm}^2 \text{ s}^{-1}$, for the sensitivity tests. We assume a zero flux condition for both upper and lower boundaries. We set the depth of the lower boundary so that thermochemical equilibrium is maintained there (typically 1000 bar, depending on the thermal state of the deep atmosphere and K_{zz}). We

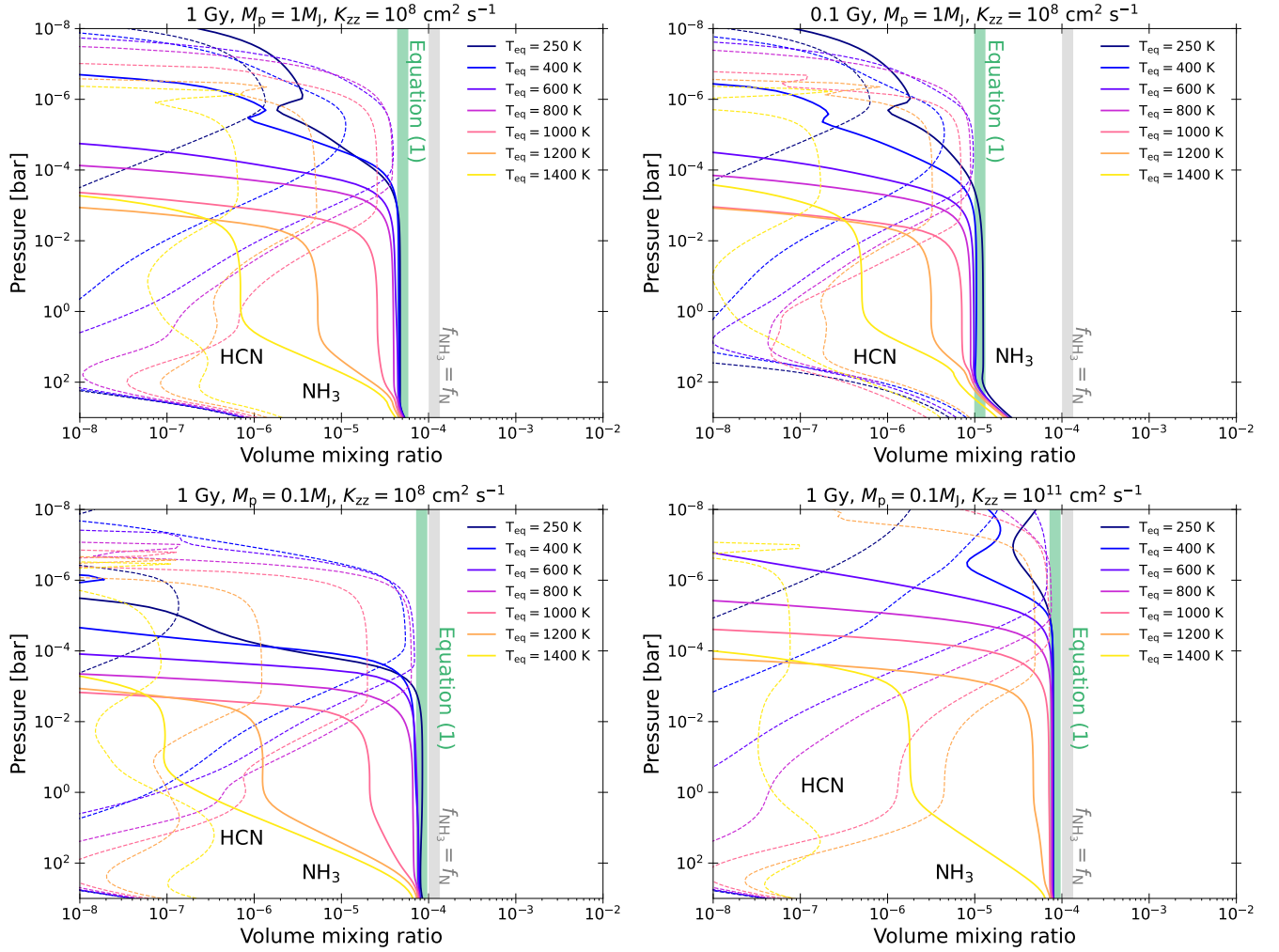


Figure 2. Vertical distributions of NH_3 (solid lines) and HCN (dashed lines) volume mixing ratios. Different colored lines show the distributions for different planetary equilibrium temperature. The gray bold lines denote the abundance equal to the bulk nitrogen abundances, while the green bold lines denote the NH_3 abundance predicted by our semi-analytical model (Equation 1). We have assumed a solar composition atmosphere in this figure. The left top panel shows the results for a 1 Gy old Jupiter mass planet with $K_{zz} = 10^8 \text{ cm}^2 \text{ s}^{-1}$, the right top panel instead sets the age of 0.1 Gy to demonstrate the effect of planetary age, the left bottom panel sets $M_p = 0.1M_J$ to demonstrate the planetary mass dependence, and right bottom panel sets $K_{zz} = 10^{11} \text{ cm}^2 \text{ s}^{-1}$ to be compared with left bottom panel for showing the K_{zz} dependence.

adopt the C-H-N-O chemistry network implemented in VULCAN as a default. We assume the solar photospheric elemental abundances of Asplund et al. (2021) for fiducial simulations. To explore a range of parameter space for planetary properties shown in Figure 1, we extract the surface gravity and intrinsic temperature from the thermal evolution tracks of Fortney et al. (2007)¹ for several representative planetary masses and ages, as summarized in Table 1. Then, we compute the atmospheric P - T profiles using the “EGP” radiative-convective equilibrium model extensively used in previous

studies² (e.g., McKay et al. 1989; Marley & McKay 1999; Fortney et al. 2005, 2007, 2008; Morley et al. 2012; Marley & Robinson 2015; Thorngren et al. 2019; Gao et al. 2020; Paper I) for various planetary equilibrium temperatures. Our fiducial simulations assume the solar spectrum (Gueymard 2018), where we set the orbital distance so that the planetary equilibrium temperature (for zero Bond albedo with full heat redistribution) coincides with a specified value. We test the effects of different stellar spectra in Section 5.2. We neglect the condensation of gas molecules since the planets studied this paper are too warm to cause condensation of NH_3 and HCN (see top panel of Figure 6).

¹ Grids of the evolution tracks are available at <https://www.ucolick.org/~jfortney/models.htm>

² A Python version of the model has recently been made publicly available (Mukherjee et al. 2022a).

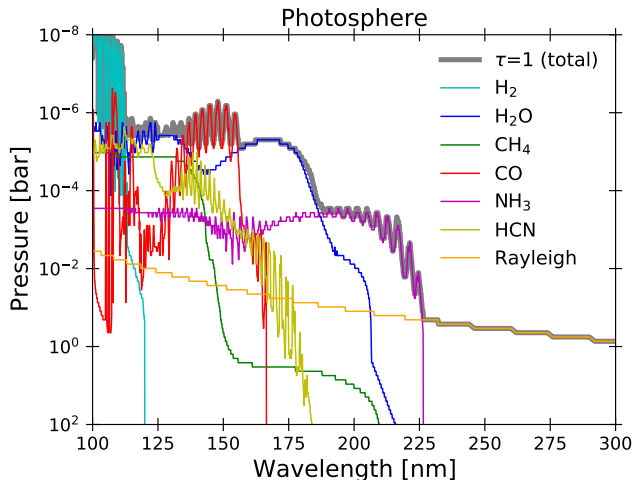


Figure 3. Photospheric pressure level of at each wavelength across the UV. The thick gray line shows the pressure level of vertical optical depth of unity, and other colored lines show the contribution of each molecule. We assume a solar composition atmosphere, $M_p = 1M_J$, age of 1 Gyr, $T_{eq} = 800$ K, and $K_{zz} = 10^8 \text{ cm}^2 \text{ s}^{-1}$.

3.2. Effects of Planetary Mass, Age, and Eddy Diffusion

We first explore how the NH_3 and HCN abundances vary with various planetary properties. Figure 2 shows the vertical distributions of NH_3 and HCN across equilibrium temperature, planetary mass, age, and eddy diffusion coefficient. In general, the NH_3 abundance is nearly constant in the middle atmosphere owing to vertical mixing, while it decreases with increasing altitudes in the upper atmosphere due to photodissociation. This general trend is in agreement with previous studies (e.g., Moses et al. 2011; Line et al. 2011; Miller-Ricci Kempton et al. 2012; Kawashima & Ikoma 2018). As predicted in Section 2, the quenched NH_3 abundances in middle atmospheres are nearly independent of the equilibrium temperature at $T_{eq} \lesssim 800$ K. For $T_{eq} \gtrsim 1000$ K, the NH_3 abundance gradually decreases with decreasing pressure at $P \sim 1$ –100 bar because of the efficient thermochemical conversion to N_2 due to high temperatures. This trend is consistent with previous studies of hot Jupiters (Moses et al. 2011).

The ratio of the quenched NH_3 to bulk nitrogen abundance depends on planetary mass and age. The gray bold lines in Figure 2 denote the bulk nitrogen abundance f_N . For Jupiter-mass planets ($M_p = 1M_J$) at 1 Gyr age (left top panel of Figure 2), the quenched NH_3 abundance is lower than the bulk nitrogen abundance by a factor of ~ 2 . The depletion factor even reaches a factor of ~ 10 for an age of ~ 0.1 Gyr (right top panel of Figure 2). On the other hand, the NH_3 abundance is almost equal to the bulk nitrogen abundances for Neptune mass planets ($M_p = 0.11M_J$) at 1 Gyr (left bottom panel of Figure 2). These results are consistent with our prediction made in the previous section (Figure 1). Thus, higher plan-

etary mass and younger age do act to deplete the quenched NH_3 as compared to the bulk nitrogen abundance.

It is worth noting that our semi-analytical prediction of the quenched NH_3 abundance (Equation 1) matches the numerical results quite well. The green bold lines in Figure 2 show the NH_3 abundance given by Equation (1), which coincides with the quenched NH_3 abundance below the NH_3 photodissociation base. Thus, even if the planetary mass and age fall into the regime where NH_3 depletion is expected, one may still be able to use our semi-analytic diagnostic model (Equation 4) to give a first-order estimate on the bulk nitrogen abundance from the NH_3 abundance.

Of course photochemistry may substantially deplete the observable NH_3 abundances at low pressure. As seen in the results for an eddy diffusion coefficient of $K_{zz} = 10^8 \text{ cm}^2 \text{ s}^{-1}$ (upper panels and lower left panel of Figure 2), the NH_3 abundance drops off at $P \lesssim 10^{-3}$ – 10^{-4} bar through photodissociation. This pressure level is significantly deeper than the pressure level where the many other chemical species experience photodissociation, say $\sim 10^{-5}$ – 10^{-6} bar. This difference is because NH_3 is fragile to UV photons to relatively longer wavelengths. To demonstrate this, Figure 3 shows the photospheric pressure level at UV wavelengths. While UV photons at $\lesssim 190$ nm are mostly absorbed by other chemical species, such as H_2O , at $\sim 10^{-5}$ – 10^{-6} bar, near-UV photons at 190–220 nm penetrate to deeper atmospheres because of negligible photolysis cross sections of other molecules. Those near-UV photons largely act to deplete NH_3 at $\sim 10^{-3}$ bar, which explains why NH_3 is vulnerable to photochemistry at relatively higher pressures. We refer readers to Hu (2021) for extended discussions on the depletion of NH_3 through photodissociation in middle atmosphere regions. We note that our simulations do not account for the presence of aerosols, such as photochemical hazes, while it may act to prevent UV photons from penetrating to deep atmospheres, as discussed in Section 5.1.

The strength of eddy diffusion affects where the photochemical depletion of NH_3 takes place. The left and right bottom panels of Figure 2 show the results for $M_p = 0.11M_J$ and 1 Gyr but for $K_{zz} = 10^8$ and $K_{zz} = 10^{11} \text{ cm}^2 \text{ s}^{-1}$. Higher K_{zz} results in the quenched NH_3 abundance continuing to higher altitudes, as the fast eddy diffusion can more easily compensate against the NH_3 loss by photodissociation (see also Hu 2021). On the other hand, different values of K_{zz} have negligible impacts on the quenched abundance of NH_3 , in agreement with previous studies (Zahnle & Marley 2014; Fortney et al. 2020).

Once the photolysis of NH_3 sets in, most of NH_3 is converted to HCN in the upper atmosphere for the equilibrium temperature of $T_{eq} = 400$ –1400 K. In Figure 2, one can notice that HCN abundances at upper atmospheres, say $P \lesssim 10^{-3}$ – 10^{-4} bar, are approximately the same as the

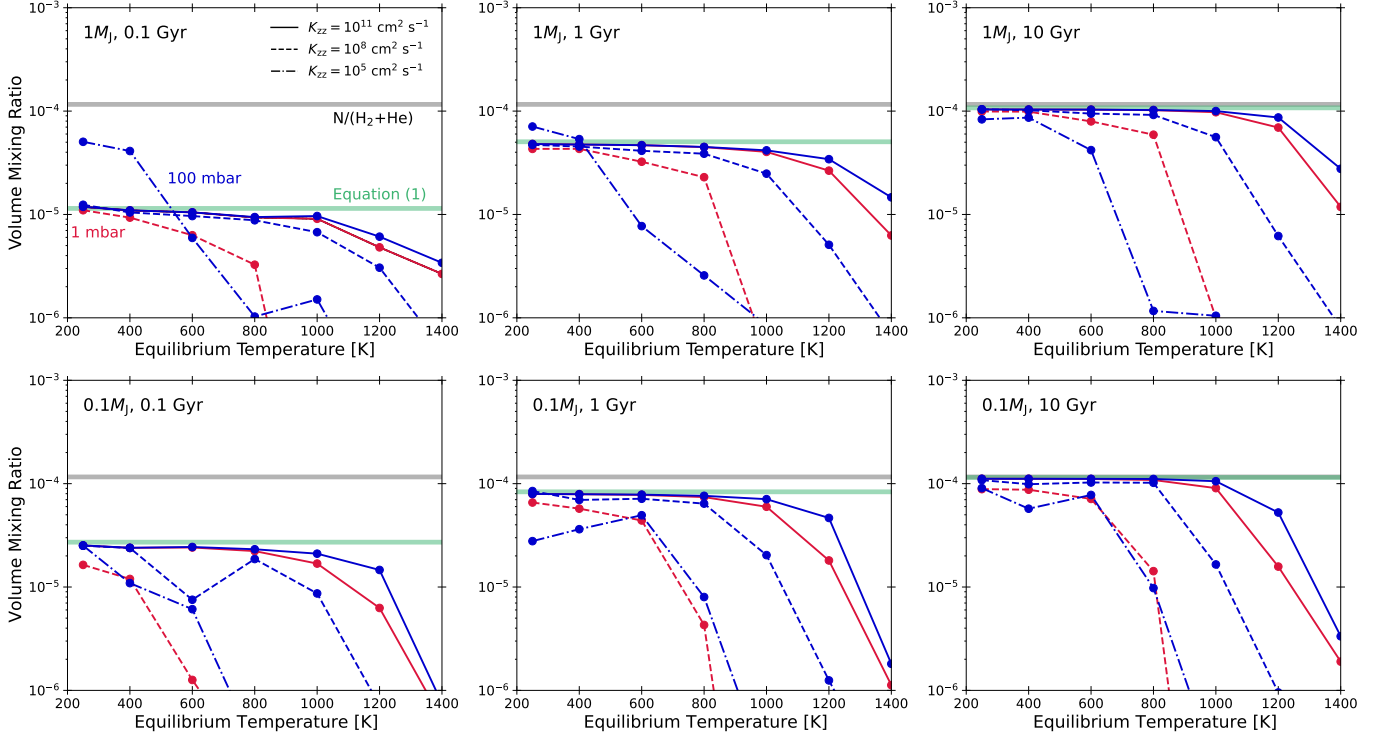
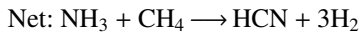
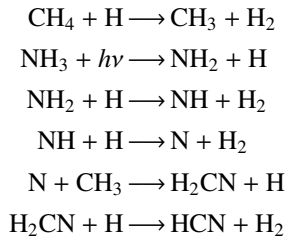


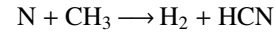
Figure 4. NH_3 abundance at pressure levels of 1 mbar (red lines) and 100 mbar (blue lines). The solid, dashed, and dash-dot lines show the abundances for $K_{zz} = 10^{11}$, 10^8 , and $10^5 \text{ cm}^2 \text{ s}^{-1}$, respectively. From left to right, each panel show the abundances for planets at the age of 0.1, 1, and 10 Gyr. The top and bottom panels show the results for Jupiter-mass ($1M_J$) and Neptune-mass ($0.11M_J$) planets, respectively. The gray lines denote the bulk nitrogen abundance, and the green lines denote the quenched nitrogen abundance predicted by Equation 1. We have assumed solar composition atmospheres.

NH_3 abundances below the photodissociation base. This result indicates that the photodissociated NH_3 is almost completely converted to HCN. Thus, one might be able to evaluate the bulk nitrogen abundance from the measurement of HCN abundance even if photodissociation significantly depletes NH_3 at pressure levels probed by observations. If the abundance profiles of NH_3 and HCN are constrained simultaneously, it would provide complementary information to infer the bulk nitrogen abundance.

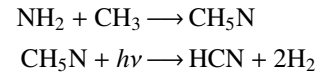
Although the detailed analysis of atmospheric chemistry is beyond the scope of this paper, we here briefly introduce HCN synthesis processes. HCN can be produced through photodissociation of NH_3 under the presence of CH_4 . For example, Moses et al. (2011) and Line et al. (2011) identified the following channel of HCN production:



HCN synthesis initiating from NH_3 photodissociation requires CH_3 produced through the reaction of CH_4 with H, where H can be provided by the photodissociation of NH_3 . In addition to the above channel through H_2CN , HCN can also directly form from N and CH_3 as (Kawashima & Ikoma 2018; Hobbs et al. 2019)



On the other hand, for temperate to cold planets, Hu (2021) identified the following channels without bypassing NH:



though CH_5N photodissociation does not actually directly yield HCN but yield CH_3NH that subsequently yield CH_2NH and HCN via reaction with atomic H and photodissociation (see Section 3.2 of Moses et al. 2010). As seen those examples, the major reaction pathway of HCN production may depend on specific photochemical model used. HCN is destroyed either by the reaction of $\text{HCN} + \text{H} \rightarrow \text{CN} + \text{H}_2$ or photodissociation of $\text{HCN} + h\nu \rightarrow \text{CN} + \text{H}$, but CN quickly reacts with H_2 to reproduce HCN again (Moses et al. 2011). In our calculations, the $\text{H}_2\text{CN} + \text{H}$ channel dominates over the $\text{N} + \text{CH}_3$ channel. The relative importance of the CH_5N

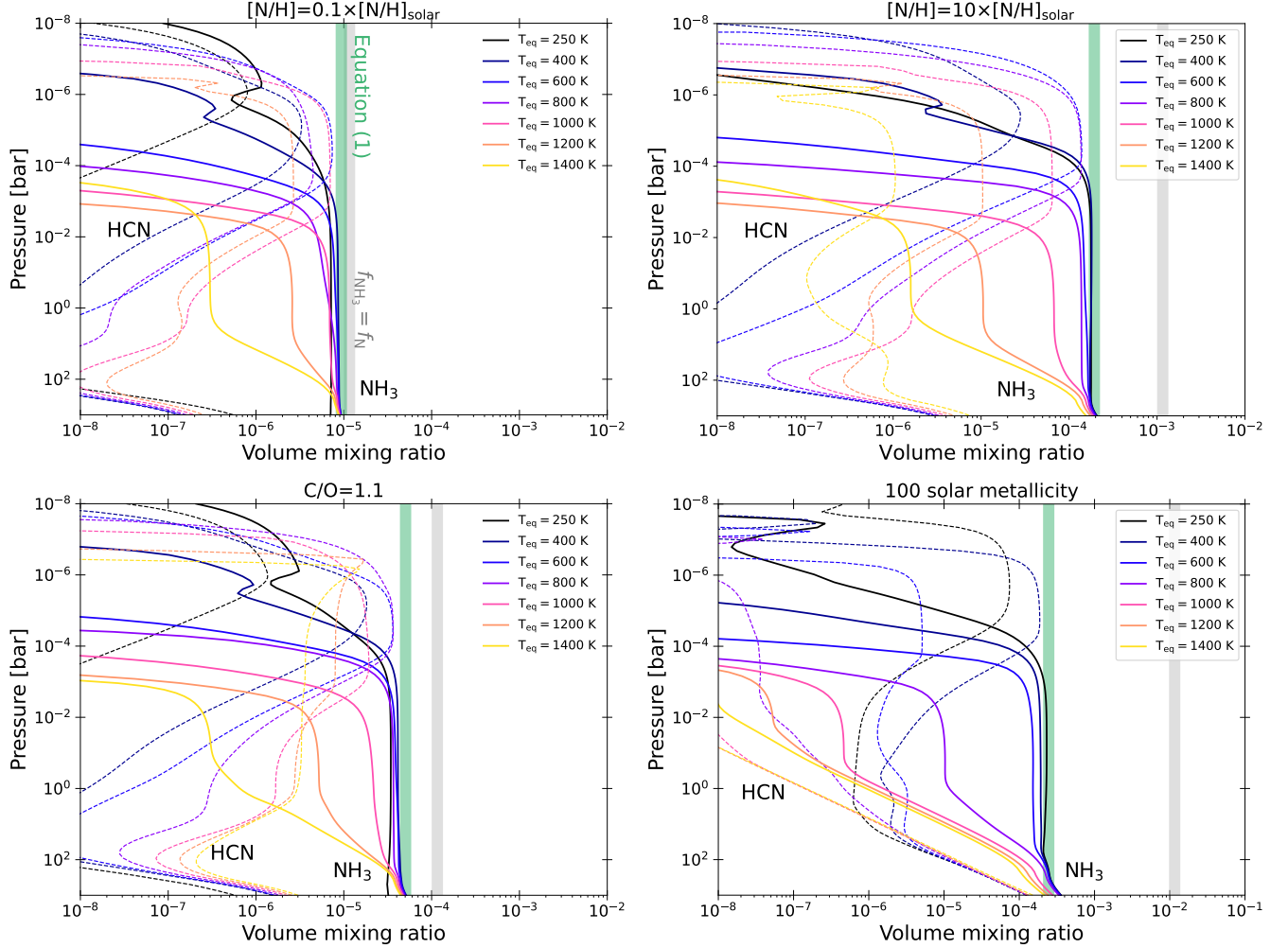


Figure 5. Same as Figure 2, but for different atmospheric compositions. The upper left and right panels show the NH_3 (solid curves) and HCN (dashed curves) distributions for the N/H ratio of $0.1\times$ and $10\times$ solar values, the lower left panel show the results for $\text{C}/\text{O}=1.1$, and the lower right panel shows the results for the atmospheric metallicity of $100\times$ the solar value. We assume a Jupiter-mass planet at the age of 1 Gyr for the variation of N/H and C/O , while we assume a Neptune-mass planet for the $100\times$ solar atmospheres. We set $K_{zz} = 10^8 \text{ cm}^2 \text{ s}^{-1}$ for all calculations.

channel in warm exoplanets remains unclear since the default chemical network of the VULCAN does not involve reactions around CH_5N (see Tsai et al. 2021b). Nevertheless, we predict that the addition of the CH_5N channel would barely affect our results in terms of HCN vertical distributions. This is because the HCN production rate is eventually limited by the upward flux of NH_3 in the limit of fast HCN synthesis, and complete conversion of NH_3 to HCN in Figure 2 implies that the HCN synthesis is already limited by the upward NH_3 flux owing to fast chemical conversion.

Figure 4 summarizes NH_3 abundances at $P = 1$ mbar and 100 mbar, which mimics the pressure levels probed by transmission and emission spectra, respectively, for various planetary masses, age, and K_{zz} . Overall, NH_3 abundances are nearly invariant with T_{eq} at temperate to warm exoplanets, which confirms the finding of Fortney et al. (2020). Beyond

a certain equilibrium temperature, photodissociation depletes NH_3 from the pressure levels of interest. The threshold equilibrium temperature depends on the eddy diffusion coefficient: $T_{\text{eq}} \sim 1200 \text{ K}$ for $K_{zz} = 10^{11} \text{ cm}^2 \text{ s}^{-1}$, $T_{\text{eq}} \sim 800 \text{ K}$ for $K_{zz} = 10^8 \text{ cm}^2 \text{ s}^{-1}$, and $T_{\text{eq}} \sim 400 \text{ K}$ for $K_{zz} = 10^5 \text{ cm}^2 \text{ s}^{-1}$. Since NH_3 found at pressure levels higher than 100 mbar is more stable to photodissociation, emission spectroscopy would have an advantage to observe quenched NH_3 that is less affected by photodissociation.

3.3. Effects of different N/O , C/O , and metallicity

We have assumed solar elemental ratios of the atmosphere thus far; however, exoplanets potentially have considerable diversity in atmospheric elemental ratios. For example, the atmospheric N/O ratio can have both super-stellar and sub-stellar N/O , depending on the formation location and whether disk solids or gas dominates the atmospheric composition

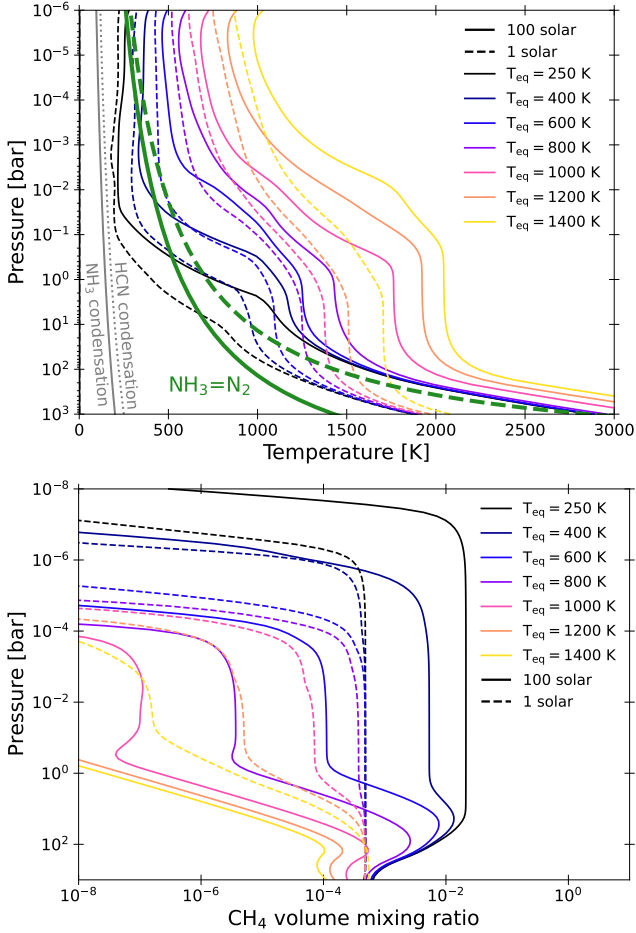


Figure 6. Atmospheric P - T profiles (top panel) and vertical distributions of CH_4 abundances (bottom panel) in a Neptune-mass planet ($0.11M_J$) with the age of 1 Gyr. Different colored lines show the profiles for different equilibrium temperature. The solid and dashed lines show the profiles for $100\times$ solar metallicity and solar composition atmospheres, respectively. The green dashed and solid lines in the top panel denote the equal equilibrium abundance P - T relation of N_2 and NH_3 , computed by the law of mass action as described in Zahnle & Marley (2014) for $\text{NH}_3 = \text{N}_2$, for solar and $100\times$ solar metallicity atmospheres, respectively. The gray solid and dotted lines in the top panel also denote the condensation temperature of NH_3 and HCN when assuming the volume mixing ratio of 10^{-4} , typical peak abundances seen in our photochemical calculations (see Figures 2 and 5), where we have used the vapor pressure of Fray & Schmitt (2009).

(e.g., Piso et al. 2016; Cridland et al. 2020; Ohno & Ueda 2021; Turrini et al. 2021; Notsu et al. 2022; Paper I). Recent retrieval studies have reported sub-solar H_2O abundances in hot Jupiter atmospheres from low-resolution (Pinhas et al. 2019; Welbanks et al. 2019) and high-resolution spectroscopy (Pelletier et al. 2021), which may be attributed to a high atmospheric C/O ratio. Several studies also suggested high metallicity atmospheres on sub-Neptunes, such as GJ1214b (e.g., Fortney et al. 2013; Morley et al. 2015;

Ohno & Okuzumi 2018; Gao & Benneke 2018; Ohno et al. 2020; Christie et al. 2022; Kempton et al. 2023; Gao et al. 2023) and GJ436b (Morley et al. 2017), and exo-Saturns, such as WASP-39b (Wakeford et al. 2018; JWST Transiting Exoplanet Community Early Release Science Team et al. 2022; Feinstein et al. 2022; Rustamkulov et al. 2022; Alderson et al. 2022; Ahrer et al. 2022; Tsai et al. 2022), WASP-117b (Carone et al. 2021), and HD149026 b (Bean et al. 2023).

We here investigate how these different atmospheric compositions affect the NH_3 and HCN vertical distributions. We test different N/O , C/O , and bulk atmospheric metallicities. We re-compute P - T profiles for different C/O and atmospheric metallicities, as such changes lead to important alternations in the P - T profile. However, for different N/O ratios we adopt the same P - T profiles as used in the previous section, as a different N/O barely affects the abundances of other O and C bearing species, such as H_2O , as long as O/H and C/H are the same (Hobbs et al. 2019). When we change N/O or C/O , we fix O/H to the solar value and change N/H or C/H to achieve the assumed N/O or C/O . Note that the atmospheric composition and P - T profile can noticeably depend on individual C/H , O/H , and N/H ratios even if C/O and N/O are the same (Drummond et al. 2019). We have fixed O/H here because we anticipate that it would be relatively easy to constrain O/H from observations, as the abundance of H_2O , a main atmospheric opacity source, is approximately proportional to O/H . We assume a Jupiter-mass planet at the age of 1 Gyr for simulations of different N/O and C/O ratios, while we assume a lower planet mass of $0.11M_J$ at the age of 1 Gyr for simulations of high atmospheric metallicity.

The quenched NH_3 abundance is sensitive to, but is not strictly proportional, to the atmospheric N/O (N/H in other words) ratio. The top two panels of Figure 5 show the vertical distributions of NH_3 and HCN abundances for $\text{N/O} = 0.1\times$ and $10\times$ solar values. The quenched NH_3 abundance is approximately 10^{-5} and 2×10^{-4} for $\text{N/O} = 0.1\times$ and $10\times$ solar values, respectively, for equilibrium temperature $\lesssim 800$ K. Recalling that the quenched NH_3 abundance is $\sim 5 \times 10^{-5}$ for the solar value of N/O (see the left top panel of Figure 2), the NH_3 abundance only varies by an order of magnitude across the two decades of N/O ratio. This relatively weak dependence on N/O ratio is due to N_2 dominating over NH_3 in the deep atmospheres for a Jupiter mass planet at 1 Gyr, as suggested by the discrepancy between NH_3 and bulk N abundances in Figures 2 and 5. Since this situation corresponds to $\mathcal{K} \ll 1$, Equation (1) indicates $f_{\text{NH}_3} \propto f_{\text{N}} \sqrt{\mathcal{K}} \propto f_{\text{N}}^{1/2}$, which explains the dependence seen in Figure 5. Thus, when N_2 likely dominates over NH_3 in the deep atmosphere, one would need precise measurements of NH_3 to well constrain the bulk nitrogen abundance. The relative importance of NH_3 and N_2 in the deep atmospheres could be inferred from the

second term of Equation (4) by inserting a retrieved NH_3 abundance into f_{NH_3} .

The higher C/O ratio only has minor effects on nitrogen chemistry. The left bottom panel of Figure 5 shows the results for C/O= 1.1. The NH_3 profile is largely similar to that for solar C/O ratio (left top panel of Figure 2). This is because an equilibrium NH_3 abundance and thus the quenched NH_3 abundance are insensitive to C/O (see Figure 6 of Moses et al. 2013b). The HCN profile in the upper atmosphere also becomes similar to that for solar C/O, as the HCN is initiated from the NH_3 photodissociation for the temperature range of our interest. However, a higher C/O acts to increase the HCN abundance at middle to deep hot atmospheres, as the thermochemistry leads to an increased HCN abundance for high C/O.

Higher atmospheric metallicity leads to more N_2 dominant atmospheres owing to two combined effects: preference of N_2 as compared to NH_3 in thermochemical equilibrium and hot deep interior due to enhanced atmospheric opacity. The right bottom panel of Figure 5 shows the results for $100\times$ solar metallicity. The quenched NH_3 abundance is $\sim 2 \times 10^{-4}$, which is approximately two orders of magnitude lower than the actual bulk nitrogen abundance. This large discrepancy is due to the fact that the high atmospheric metallicity yields hotter deep interiors. We show the P - T profiles of solar composition and $100\times$ solar metallicity atmospheres in Figure 6. The figure demonstrates that the atmospheres with $100\times$ solar metallicity yield deep adiabatic profiles much hotter than those of solar composition atmospheres, which acts to increase N_2/NH_3 ratio in the deep atmosphere. Furthermore, N_2 , a “metal-metal” species, is also strongly favored compared to NH_3 as the metallicity increases, at a given P and T (Lodders & Fegley 2002; Moses et al. 2013b). Therefore, the quenched NH_3 at $P \sim 1$ – 100 bar starts to be depleted through thermochemical conversion at a threshold temperature of $T_{\text{eq}} \sim 800$ K, which is cooler than that found in solar composition atmospheres ($T_{\text{eq}} \sim 1200$ K).

High atmospheric metallicity also impacts the HCN abundances at the upper atmosphere. While the HCN abundances at upper atmospheres are nearly the same as the quenched NH_3 abundances for solar composition atmospheres (Figure 2), for $100\times$ solar metallicity the HCN abundances are much lower than the quenched NH_3 abundances at $T_{\text{eq}} \gtrsim 600$ K. This finding owes to the depletion of CH_4 in the high metallicity atmospheres. The bottom panel of Figure 6 shows the vertical distributions of CH_4 for solar composition and $100\times$ solar metallicity atmospheres. We can see that, at $T_{\text{eq}} \gtrsim 600$ K, the high metallicity atmosphere yields much lower CH_4 abundances than those for solar composition atmospheres at $P \sim 10^{-3}$ – 10^{-4} bar, where the HCN production takes place. The CH_4 depletion is due to preference for CO over CH_4 at higher metallicity, as well as the hotter temper-

ature of the higher metallicity atmospheres. Because HCN production requires the presence of CH_4 as discussed earlier, the CH_4 depletion results in the HCN depletion at high metallicity atmospheres.

4. IMPLICATIONS FOR SPECTROSCOPIC OBSERVATIONS

4.1. Transmission spectroscopy

We next turn to the study of the observational feasibility of NH_3 and HCN in exoplanet transmission spectroscopy. We use the publicly available code CHIMERA (Line et al. 2013) to generate synthetic transmission spectra. We customize CHIMERA so that the molecular abundances of H_2O , CH_4 , CO , CO_2 , NH_3 , N_2 , HCN, C_2H_2 , C_2H_6 are extracted from the results of VULCAN. We assume thermochemical equilibrium for the remaining chemical species. We assume Jupiter-mass planets with 10 bar reference radii of 1.21 , 1.11 , and $1.04R_J$ at 0.1, 1, and 10 Gyr, respectively. These radii correspond to the surface gravities of 16.90, 19, 96, and 22.71 m s^{-2} , assumed in our photochemical calculations (see Table 1). To compute transit depths, we assume a solar radius for all spectral calculations.

The magnitudes of NH_3 and HCN features depend on the planetary equilibrium temperatures. The left top panel of Figure 7 shows the transmission spectra for different T_{eq} values. In general, NH_3 leaves relatively strong spectral features at 1.2, 1.5, 2.0, 3.0, and $11 \mu\text{m}$, while HCN leaves features only at $14 \mu\text{m}$. The NH_3 features at near-infrared wavelength are in agreement with MacDonald & Madhusudhan (2017a), whereas several unique features beyond $2 \mu\text{m}$ suggested by MacDonald & Madhusudhan (2017a) are barely seen in our spectra. This is because we mainly focus on warm exoplanets in which the spectral features of CH_4 tend to obscure the NH_3 spectral features. In our spectra relevant to hot Jupiters ($T_{\text{eq}} = 1200$ and 1400 K), the NH_3 depletion through thermochemical conversion and photodissociation significantly weakens NH_3 feature, as compared to MacDonald & Madhusudhan (2017a) who fixed the NH_3 abundance regardless of planetary equilibrium temperature.

We also conduct the same analysis for HCN; however, HCN features are almost absent in our synthetic spectra. HCN features are weak in our models because HCN is present only at low pressures ($\lesssim 10^{-3}$ bar) as HCN forms through photodissociation of NH_3 at $P \sim 10^{-3}$ – 10^{-4} bar. The magnitudes of HCN features at 3.1 and $14 \mu\text{m}$, though weak, gradually increase with increasing equilibrium temperature, as the enhanced stellar UV photons cause the HCN production at slightly higher pressures. In our model, the $3.1 \mu\text{m}$ feature is at most ~ 20 ppm, while the $14 \mu\text{m}$ feature could be larger than 50 ppm.

The NH_3 and HCN features also modestly depend on the planet’s age. The right top panel of Figure 7 shows the trans-

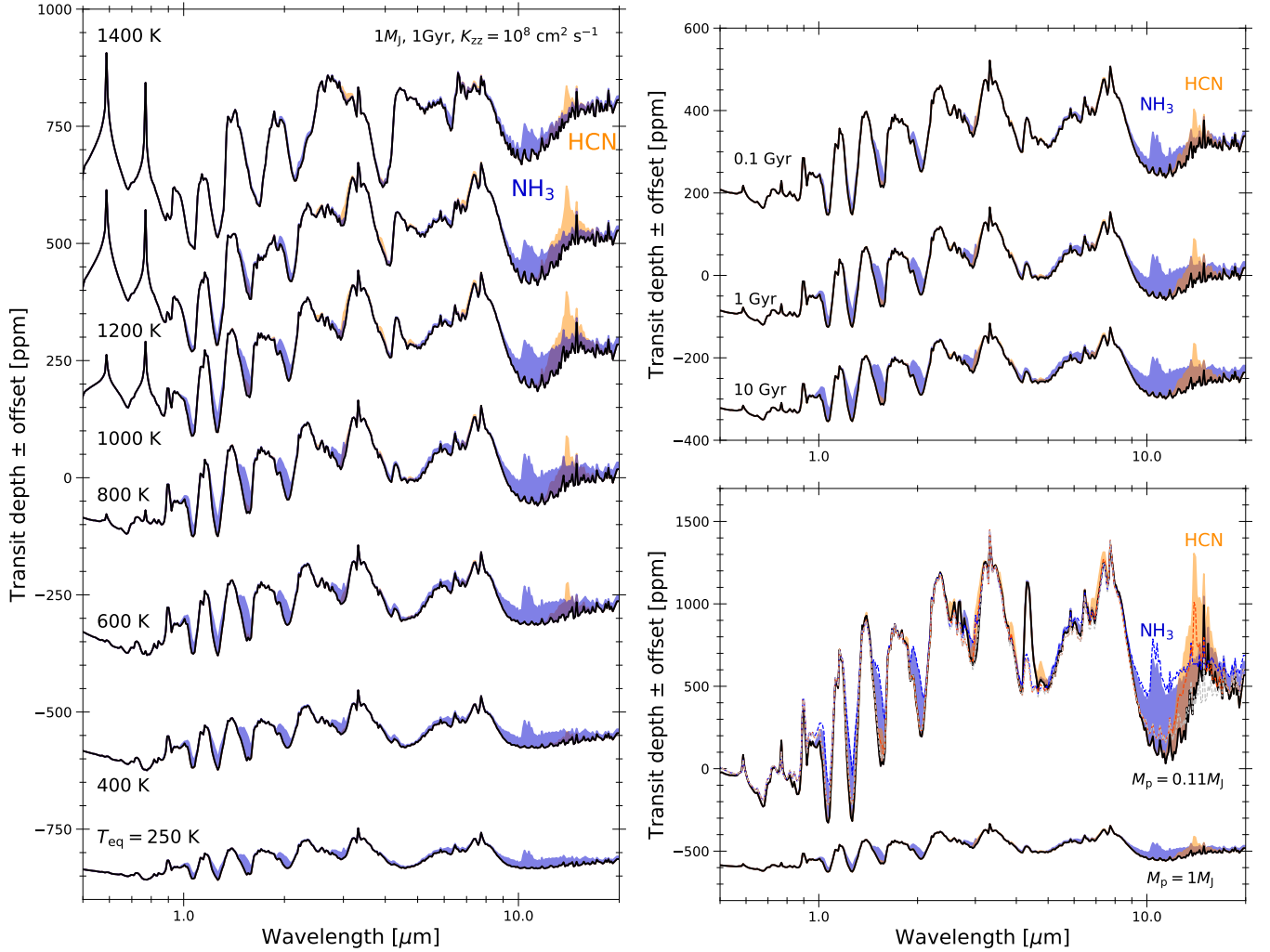


Figure 7. Synthetic transmission spectra of warm exoplanets. The left panel shows the transit depths of Jupiter-mass planets orbiting around a Sun-like star with various equilibrium temperature, where we assume 1 Gyr age. The black lines show the spectra without NH_3 and HCN , and the blue and orange shaded parts denote the excess transit depth when we include NH_3 and HCN absorption. The upper right panel shows the spectra of Jupiter-mass planets with $T_{\text{eq}} = 800$ K at different system ages. The lower right panel shows the spectra for sub-Jupiter ($M_p = 0.11 M_J$) and Jupiter mass ($1 M_J$) planets with $T_{\text{eq}} = 800$ K at 1 Gyr age. We assume solar composition atmospheres and $K_{zz} = 10^8 \text{ cm}^2 \text{ s}^{-1}$ for all spectra shown here.

mission spectra of Jupiter-mass planets with $T_{\text{eq}} = 800$ K and $K_{zz} = 10^8 \text{ cm}^2 \text{ s}^{-1}$ for different system ages. As discussed in Section 3.2, NH_3 and HCN abundances are lower at younger planets because of hotter interiors and deep atmospheres (Fortney et al. 2020). Thus, the NH_3 and HCN features tend to be weaker for younger planets. On the other hand, younger planets have lower surface gravity and larger atmospheric scale height. Because the large scale height enhances the amplitudes of spectral features and partly compensates the effect of decreased abundances of NH_3 and HCN , the magnitudes of spectral features only moderately depend on system age.

We note that, of course, the actual strength of NH_3 and HCN features depend on the planetary gravity. The right bottom panel of Figure 7 shows the spectra for the plan-

etary mass of $1 M_J$ and $0.11 M_J$, corresponding to the surface gravity of 19.96 and 3.47 m s^{-2} at 1 Gyr age (see Table 1). The $0.11 M_J$ mass planet shows much larger spectral features, including NH_3 and HCN features. This is mostly because the spectral features of transmission spectrum are scaled by atmospheric scale height (e.g., Kreidberg 2018). In fact, the two spectra agree well with each other once we rescale the $1 M_J$ planet spectrum by multiplying a factor of $19.969/3.475$, the ratio of the surface gravities (dashed lines). The different gravities still alter the spectral shapes at certain wavelength owing to differences of atmospheric composition, such as the CO_2 absorption feature at $4.3 \mu\text{m}$.

The magnitudes of NH_3 and HCN features also depend on the eddy diffusion coefficient. The left panel of Figure 8 shows the transmission spectra for different K_{zz} values.

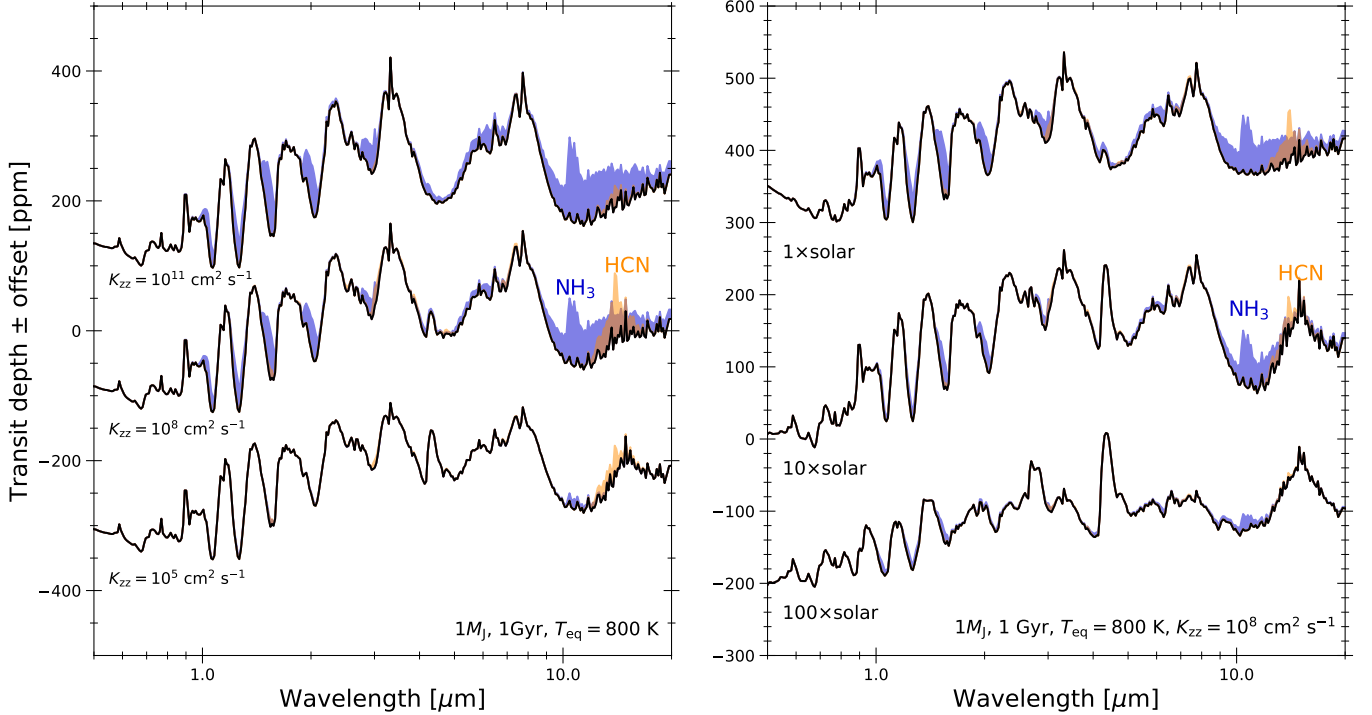


Figure 8. Transmission spectra of a 1 Gyr old Jupiter-mass planet with $T_{\text{eq}} = 800$ K around Sun-like stars for various K_{zz} values (left) and atmospheric metallicities (right).

The NH_3 features become prominent as K_{zz} increases, as a higher K_{zz} pushes the depth of the photodissociation to lower pressures. On the other hand, the HCN features have a non-monotonic dependence on K_{zz} . The HCN features become weak at high K_{zz} because HCN production, which is driven by NH_3 photodissociation, takes place at much higher altitudes than that probed by transmission spectrum. The features also become weak at very low K_{zz} , as thermochemistry tends to convert NH_3 to N_2 in the middle atmospheres before NH_3 is converted to HCN. Thus, interestingly, there is a sweet spot value of K_{zz} that maximizes the HCN features.

Atmospheric metallicity also has a strong impact on the NH_3 and HCN feature strengths. The right panel shows the spectra for the atmospheric metallicities of 1 \times , 10 \times , and 100 \times the solar value. The NH_3 and HCN features become weaker as the metallicity becomes higher. This is because the NH_3 abundance remains roughly the same as metallicity increases owing to the conversion of N into N_2 at deep atmospheres (see Paper I, Section 2, and Section 3.3) whereas other molecular abundances, such as H_2O , increase with increasing metallicity. As a result, NH_3 features tend to be embedded into the absorption features of other molecules. Meanwhile, unless the planet is as cool as $T_{\text{eq}} \lesssim 400$ K, higher atmospheric metallicity leads a lower abundance of CH_4 , which results in the depletion of HCN (Section 3.3, see also Figure 6). Thus, observations of NH_3 and HCN are more challenging for higher metallicity atmospheres.

4.2. Emission spectroscopy

We investigate the observational feasibility of NH_3 and HCN in emission spectroscopy as well. As in the previous section, we use the CHIMERA to compute synthetic emission spectra for hypothetical Jupiter-mass planets around sun-like star, where the stellar spectrum is taken from the PHOENIX grid (Husser et al. 2013) for stellar effective temperature of $T_{\text{eff}} = 5780$ K, metallicity of $[M/H] = 0$, and gravity of $\log(g) = 4.43$.

The NH_3 features in the emission spectra are maximized at warm exoplanets with $T_{\text{eq}} \sim 600\text{--}1000$ K, similar to transmission spectroscopy. Figure 9 shows the emission spectra for various equilibrium temperatures. The emission spectra always exhibit the strongest NH_3 feature around $11 \mu\text{m}$ followed by the feature around $\sim 6 \mu\text{m}$. The features at longer wavelengths are more noticeable because of the more favorable planet-to-star flux contrast. Since the planetary emitting flux is intrinsically weaker at cooler planets, as seen in the $T_{\text{eq}} = 400$ K case, the cooler planets have weaker NH_3 features if we assume the same stellar properties. On the other hands, hotter planets emit more flux but have a lower NH_3 abundance owing to thermal conversion, which also results in weaker NH_3 features as seen in the cases of $T_{\text{eq}} = 1200$ and 1400 K.

The system age moderately affects NH_3 and HCN features in emission spectra. The upper three right panels of Figure 9 show the spectrum of a Jupiter-mass planet with $T_{\text{eq}} = 800$ K

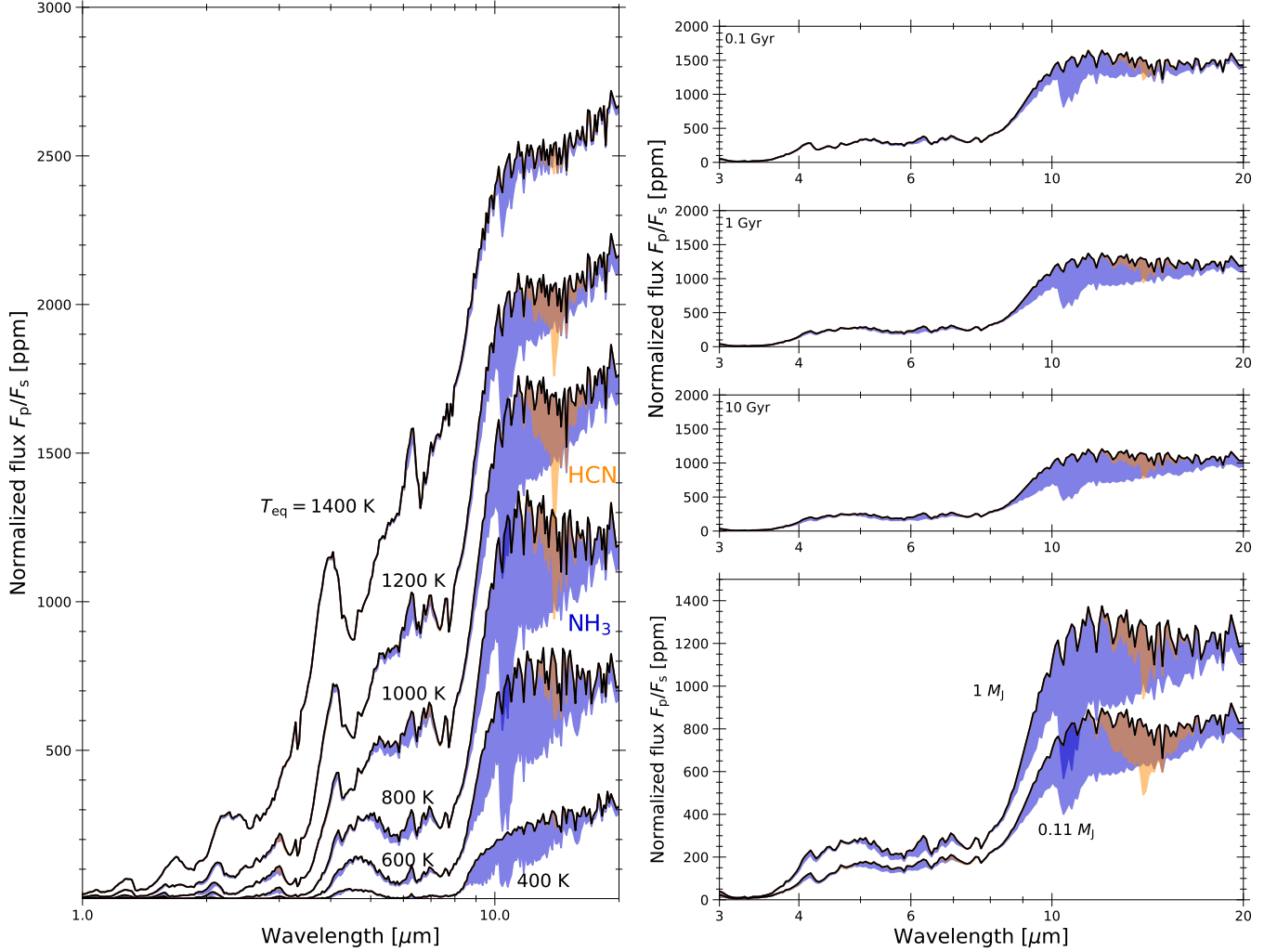


Figure 9. Synthetic emission spectra of giant planets around a Sun-like star. The black lines show the spectra without NH_3 and HCN , and the blue and orange shaded parts denote the reduction of planetary thermal emission when we include NH_3 and HCN absorption. The left panel shows the spectra of Jupiter-mass planets at 1 Gyr age for various planetary equilibrium temperature. The right top three panels show the spectra of Jupiter-mass planets with $T_{\text{eq}} = 800$ K at different ages. The right bottom panel shows the spectra for $T_{\text{eq}} = 800$ K and 1 Gyr age at different planetary masses. We have assumed solar composition atmospheres and $K_{zz} = 10^8 \text{ cm}^2 \text{ s}^{-1}$ for all spectra presented here.

at 0.1, 1, and 10 Gyr. The planet at 0.1 Gyr has relatively weak NH_3 feature because their hot deep atmospheres convert NH_3 into N_2 efficiently. On the other hand, the planetary emission itself becomes stronger at younger ages owing to the hot deep atmosphere.

The strength of NH_3 feature also depends on the eddy diffusion coefficient. The left columns of Figure 10 show how the strength of NH_3 and HCN features vary with K_{zz} for a 1 Gyr old Jupiter-mass planet with $T_{\text{eq}} = 800$ K. The spectral shape is nearly the same between $K_{zz} = 10^{11}$ and $10^8 \text{ cm}^2 \text{ s}^{-1}$. This is because the quenched NH_3 abundance is insensitive to K_{zz} (Saumon et al. 2006; Zahnle & Marley 2014; Fortney et al. 2020; Paper I), and emission spectra probe the pressure level below the NH_3 photodissociation base at $K_{zz} = 10^8 \text{ cm}^2 \text{ s}^{-1}$. Thus, the further elevation of the photodissociation base by high K_{zz} no longer affects the

strength of NH_3 feature. NH_3 features become weaker at very low value of $K_{zz} = 10^8 \text{ cm}^2 \text{ s}^{-1}$ because thermochemistry converts NH_3 to N_2 at the pressure level probed by emission spectra.

Atmospheric metallicity substantially affects the strength of NH_3 and HCN features. The right columns of Figure 10 show the emission spectra at $1\times$, $10\times$, and $100\times$ solar metallicity. The NH_3 and HCN feature becomes weaker at the higher atmospheric metallicity owing to the thermochemical conversion of NH_3 into N_2 at deep atmospheres, which results in the depletion of NH_3 and HCN at upper atmospheres. This trend is the same as that seen in the transmission spectroscopy. However, while the high metallicity weakens the entire spectral features for transmission spectrum, the high metallicity instead enhance planetary emission by warming the atmosphere.

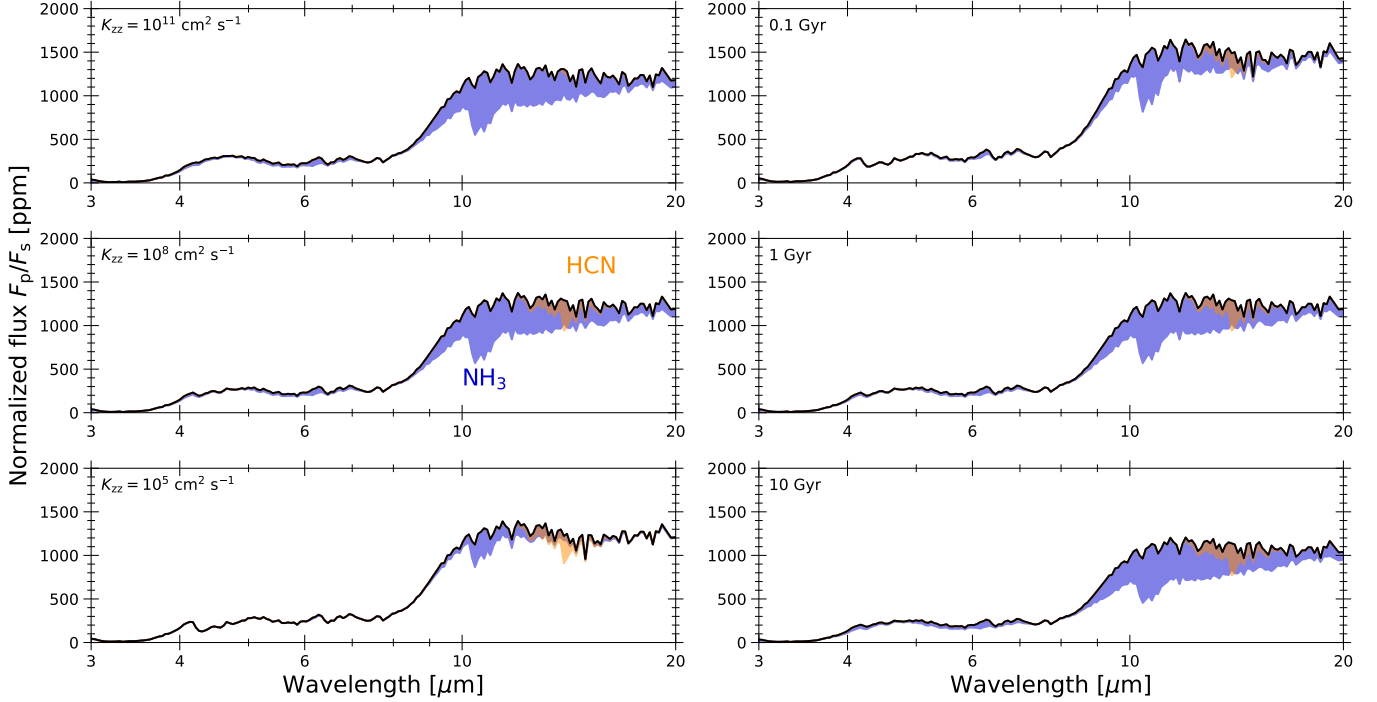


Figure 10. Emission spectra of 1 Gyr old Jupiter-mass planets with $T_{\text{eq}} = 800$ K around Sun-like stars for various values of eddy diffusion strength K_{zz} (left column) and atmospheric metallicity (right column).

As in the transmission spectra, HCN features are relatively weak compared to NH_3 features. Only the feature around $14 \mu\text{m}$ is noticeable. The relatively weak HCN feature can be attributed to the vertical distribution of HCN. The emission spectrum probes deeper in the atmosphere than the transmission spectrum, while HCN is mainly produced by photochemistry in the upper atmosphere. This spatial separation between the HCN production region and observationally sensitive region results in the relatively weak HCN features in the emission spectrum.

4.3. Observational Feasibility of NH_3 and HCN

We quantify the observational feasibility of NH_3 by examining the difference in spectrum with NH_3 and without nitrogen species (i.e., NH_3 and HCN). For transmission spectra, we define the strength of NH_3 features as

$$\Delta \left(\frac{R_p}{R_s} \right)_{\text{NH}_3}^2 = \left(\frac{R_p}{R_s} \right)_{\text{w/ NH}_3}^2 - \left(\frac{R_p}{R_s} \right)_{\text{w/o NH}_3\&\text{HCN}}^2. \quad (6)$$

This approach is similar to MacDonald & Madhusudhan (2017a). For emission spectra, the strength is defined as

$$\Delta \left(\frac{F_p}{F_s} \right)_{\text{NH}_3} = \left(\frac{F_p}{F_s} \right)_{\text{w/o NH}_3\&\text{HCN}} - \left(\frac{F_p}{F_s} \right)_{\text{w/ NH}_3}. \quad (7)$$

We compute the above metric at wavelength for various planetary equilibrium temperatures assuming a Jupiter-mass planets around a Sun-like star at 1 Gyr age, with a solar composition atmosphere and $K_{zz} = 10^8 \text{ cm}^2 \text{ s}^{-1}$. We note that the

actual feature strength depends on stellar and planetary properties; for example, the feature strengths of the transmission spectrum are enhanced for smaller stars and/or lower gravity planets with larger scale heights. Our objective here is to explore the optimum range of wavelength and planetary equilibrium temperature for detecting NH_3 under the same system conditions. The same analysis is also carried out for HCN.

The left column of Figure 11 shows the NH_3 and HCN feature strengths of the transmission spectrum as a function of wavelength and equilibrium temperature. In the transmission spectra, NH_3 leaves relatively strong spectral features at 1.5 , 2.0 , and $11.0 \mu\text{m}$. These features could be relatively strong, at an amplitude of > 50 ppm (black contours), at equilibrium temperatures from ~ 400 – 1000 K. Since the observational noise floor was anticipated to be 20 – 50 ppm (Greene et al. 2016), the result suggests that NH_3 could be identified in the near infrared with JWST. The unique NH_3 feature at $11.0 \mu\text{m}$, accessible to JWST MIRI, would be particularly useful to identify NH_3 , as the feature is present in an opacity window of H_2O and CH_4 and atmospheric clouds/hazes tend to be optically thin at longer wavelengths. In general, warm (~ 400 – 1000 K) exoplanets are optimum targets for detecting NH_3 because hot planets tend to experience NH_3 depletion by both thermochemistry and photochemistry whereas cold planets suffer from weak spectral features owing to small atmospheric scale heights.

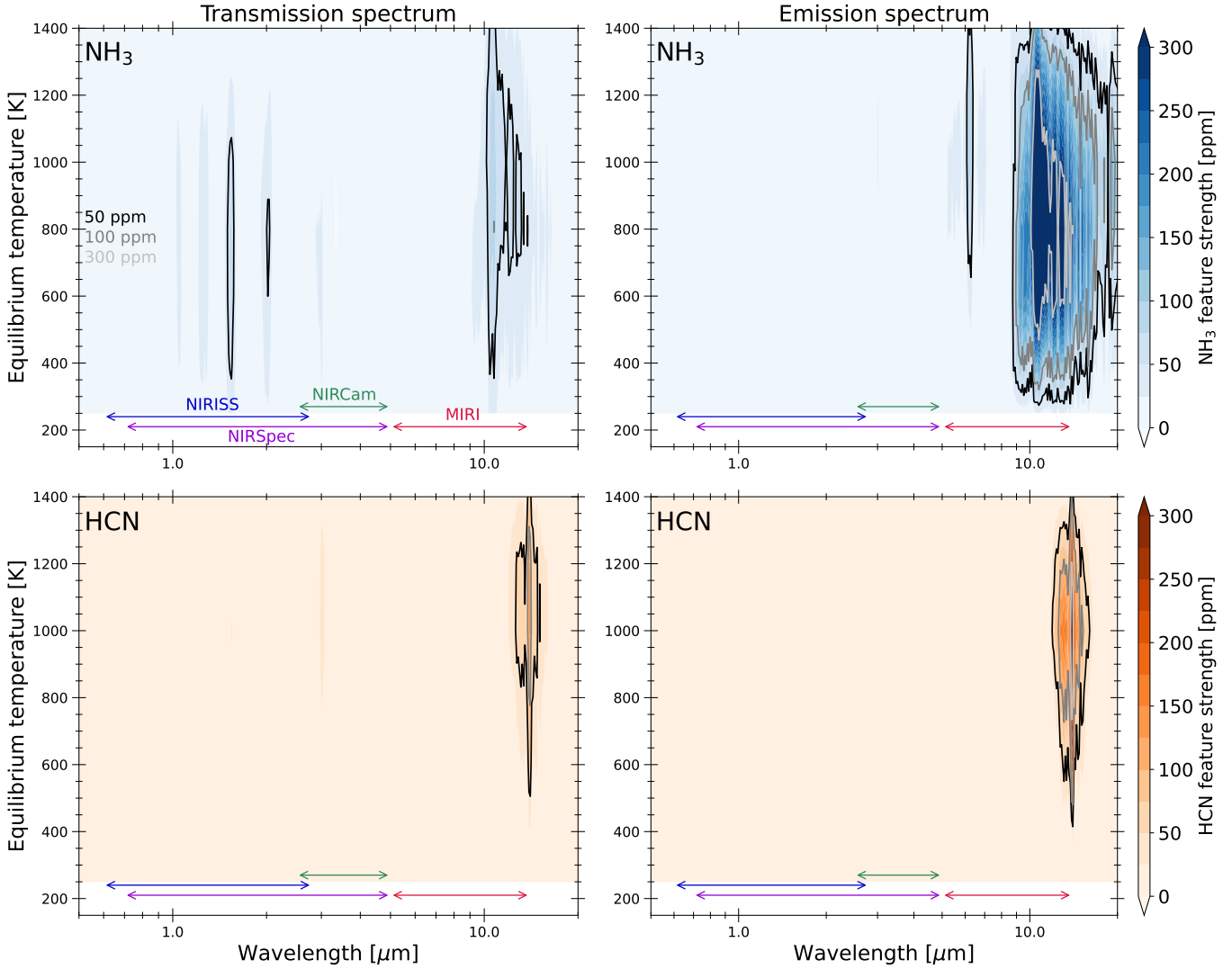


Figure 11. Strength of NH_3 (top row) and HCN (bottom row) absorption features as a function of wavelength and planetary equilibrium temperature (see Section 4.3 for definition of the feature strength). The left and right columns show the results for transmission and emission spectra, respectively. The black, gray, and silver lines denote the contours of 50, 100, and 300 ppm, respectively. The colored arrows at the bottom of each panel denote the wavelength range of JWST NIRISS (0.6–2.8 μm), NIRCam (2.5–5 μm), NIRSpec (0.7–5 μm), and MIRI (5–14 μm), taken from Batalha et al. (2017). We have assumed a Jupiter-mass planet around a Sun-like star at 1 Gyr age with a solar composition atmosphere and $K_{zz} = 10^8 \text{ cm}^2 \text{ s}^{-1}$.

Although the NH_3 feature strength of the transmission spectra is at most ~ 50 ppm for Jupiter-mass planets around Sun-like stars, the emission spectrum could show much larger NH_3 features for the same conditions. The right column of Figure 11 shows the NH_3 and HCN feature strength for emission spectra. In emission, NH_3 leaves a moderately strong feature at $\sim 6 \mu\text{m}$ and very prominent feature at $\sim 11 \mu\text{m}$. In particular, the $11 \mu\text{m}$ feature strength exceeds 300 ppm at $T_{\text{eq}} \sim 400\text{--}1200$ K, meaning that the NH_3 feature is more than 6 times larger than the noise floor of JWST-MIRI anticipated by Greene et al. (2016). Although the observational noise tends to be large at such long wavelength owing to the decreased number of stellar photons, given the

prominence of feature and expectation for low cloud and haze opacity, emission spectroscopy by JWST-MIRI would offer a viable window to search for NH_3 in wide range of the equilibrium temperatures through the $11 \mu\text{m}$ feature.

Our model predicts that HCN features are very weak at a wide range of wavelengths and equilibrium temperatures. In both transmission and emission spectra, the HCN feature strength is smaller than 50 ppm over the entire T_{eq} range explored by this study (250–1400 K), except for the feature around $14 \mu\text{m}$ whose feature strength could be as large as 50 ppm for transmission and 300 ppm for emission spectra. Thus, the observation by JWST-MIRI may still be able to find a hint of HCN feature in addition to the NH_3 feature. On

the other hand, if future observations detect prominent HCN features at $< 10 \mu\text{m}$, it potentially indicates that the atmospheric composition is significantly different from the solar composition assumed in these figures. For example, a very high C/O ratio ($\text{C/O} \gg 1$) increases HCN abundance by orders of magnitude (Moses et al. 2013a; Hobbs et al. 2021), which may yield noticeable HCN features at short wavelengths.

5. DISCUSSION

5.1. Effects of Photochemical Haze

We have assumed clear atmospheres in this study; however, recent studies suggested that warm exoplanets are universally veiled by photochemical hazes (e.g., Crossfield & Kreidberg 2017; Gao et al. 2020; Dymont et al. 2021). Photochemical hazes can affect our results in multiple ways, including flattening spectral features that limits the observability of atmospheric molecules (e.g., Fortney 2005; Morley et al. 2013; Lavvas & Koskinen 2017; Kawashima & Ikoma 2018, 2019; Adams et al. 2019; Lavvas et al. 2019; Ohno & Kawashima 2020; Gao & Zhang 2020; Steinrueck et al. 2021, 2023; Ohno & Tanaka 2021; Arfaux & Lavvas 2022).

An additional intriguing effect is that hazes alter the energy balance and P - T profiles significantly (Morley et al. 2015; Lavvas & Arfaux 2021; Arfaux & Lavvas 2022; Steinrueck et al. 2023). For example, Molaverdikhani et al. (2020) suggested that (though they focused on radiative feedback of mineral clouds) thick clouds may cause hot deep atmospheres and deplete NH_3 . The consequence of radiative feedback of photochemical haze is not trivial. The hazes heat upper atmospheres by absorbing stellar flux (Morley et al. 2015; Lavvas & Arfaux 2021), which may deplete NH_3 via thermochemical conversion. On the other hand, the hazes cool lower atmospheres by blocking stellar light from reaching the deeper atmosphere (Morley et al. 2015), which may act to maintain the quenched NH_3 abundance by suppressing the thermochemical conversion of NH_3 to N_2 .

Hazes also shield atmospheres from stellar UV photons and may alter photochemistry. Sagan & Chyba (1997) and Wolf & Toon (2010) suggested that photochemical hazes could shield NH_3 from solar UV photons in the Archean Earth, which might help to maintain warm climates. If similar processes work at warm exoplanets, hazes may help to stabilize NH_3 against photodissociation. Overall haze effects depend on particle properties, such as particle size and shapes, which are controlled by microphysical process. We will comprehensively investigate the overall impacts of photochemical hazes on atmospheric structure and chemistry in future work.

5.2. Effects of Stellar Spectral Type

While we have assumed the solar spectrum for the photochemical modeling, different stellar spectra could affect the

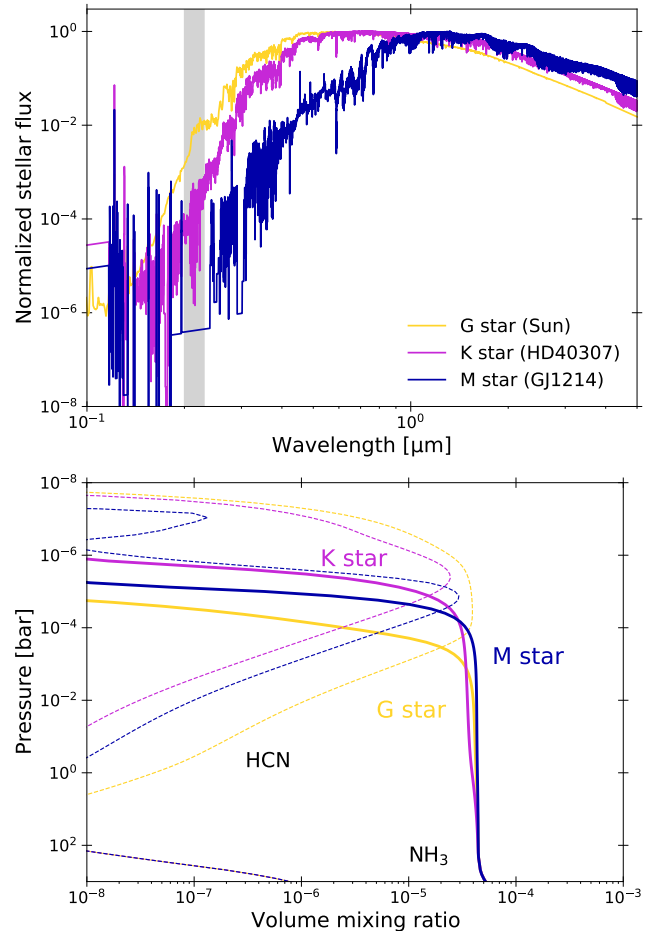


Figure 12. (Top) Stellar spectra λF_{λ} at the stellar surface. The yellow, magenta, and navy lines show the spectra of G-type (Sun), K-type (HD40307), and M-type (GJ1214) stars, respectively. The flux are normalized by the maximum value. The gray shaded region denotes the wavelength band of 200–230 nm, which mainly drives NH_3 photodissociation. (Bottom) Vertical distributions of NH_3 (solid lines) and HCN (dashed lines) on warm planets around the different spectral type stars listed in the top panel. We assume a Jupiter-mass planet with age of 1 Gyr, $T_{\text{eq}} = 600 \text{ K}$, and $K_{\text{zz}} = 10^8 \text{ cm}^2 \text{ s}^{-1}$.

results, especially for the photochemical depletion of NH_3 . Indeed, Hu (2021) studied photochemistry in three temperature and cold exoplanets, K2-18b, PH2 b, and Kepler-167 e, and found that photodissociation of NH_3 is insignificant on planets around M stars as compared to those around G/K stars (see also Baeyens et al. 2022 for the effects of stellar spectral type in pseudo-2D photochemical simulations). This was attributed to the low UV flux of M-type stars at 200–230 nm that mainly cause the photodissociation of NH_3 (Hu 2021, see also Section 3.2). Figure 12 shows the stellar spectra of G-, K-, and M-type stars, where we use a solar spectrum of Gueymard (2018) as an analog of a G-type star, the spectrum of HD40307 ($T_{\text{eff}*} = 4867 \text{ K}$, $R_* = 0.716R_{\odot}$, Stassun

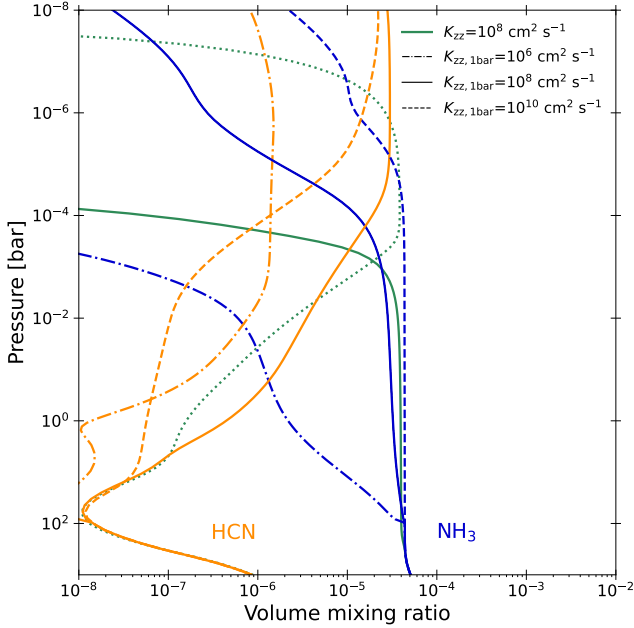


Figure 13. Vertical distributions of NH_3 and HCN for different parameterizations of K_{zz} . The blue and orange dash-dot, solid, dashed lines show the vertical distribution of NH_3 and HCN for vertically varying K_{zz} with $K_{zz, 1\text{bar}} = 10^6, 10^8,$ and $10^{10} \text{ cm}^2 \text{ s}^{-1}$, respectively. The green solid and dotted lines show the distributions for vertically constant $K_{zz} = 10^8 \text{ cm}^2 \text{ s}^{-1}$ for reference. We have assumed a Jupiter mass planet with a solar composition atmosphere, $T_{\text{eq}} = 800 \text{ K}$, and 1 Gyr age.

et al. 2019) as an analog of a K-type star, and GJ1214 as an analog of a M-type star ($T_{\text{eff}*} = 3250 \text{ K}$, $R_* = 0.215R_{\odot}$, Cloutier et al. 2021). The latter two spectra are measured by the MUSCLES Treasury Survey³ (France et al. 2016; Youngblood et al. 2016; Loyd et al. 2016). The cooler the star is, the weaker UV flux from 200–230 nm, which potentially lessens NH_3 depletion by photodissociation.

To investigate the effects of stellar spectral type, we perform additional photochemical calculations for G-, K-, and M-type stars shown in the top panel of Figure 12. To isolate the effects of stellar spectral type on photochemistry, we use the same P - T profile of a Jupiter-mass planet with $T_{\text{eq}} = 600 \text{ K}$ at 1 Gyr (for the effects of stellar spectral type on P - T profiles, see Mollière et al. 2015; Fortney et al. 2020). We also adjust the orbital distance d so that the stellar flux on the top of atmosphere is consistent with the assumed equilibrium temperature, as

$$d = \frac{1}{2} R_* \left(\frac{T_{\text{eff}*}}{T_{\text{eq}}} \right)^2. \quad (8)$$

We confirm that NH_3 could be more stable against photodissociation at cooler stars. The bottom panel of Figure

12 shows the vertical distributions of NH_3 and HCN on the planet around G-, K-, and M-type stars. As expected, NH_3 retains the quenched abundance until $\sim 10^{-5} \text{ bar}$ for K- and M-type stars, which is approximately an order of magnitude lower than the pressure level where photodissociation takes place for G-type stars. Thus, we suggest that warm planets around K-type and M-type stars are ideal targets for detecting NH_3 , as the photodissociation of NH_3 would be relatively insignificant.

5.3. Previous Observations of NH_3 on Exoplanets

Thus far there have been three exoplanets for which NH_3 absorption was reported: the canonical transiting hot Jupiter HD 209458b ($T_{\text{eq}} = 1484 \text{ K}$, Giacobbe et al. 2021) and warm Jupiters WASP-80b ($T_{\text{eq}} = 817 \text{ K}$, Carleo et al. 2022) and WASP-69b ($T_{\text{eq}} = 963 \text{ K}$, Guilluy et al. 2022), the latter two planets fall in the temperature regime where NH_3 features are expected to be relatively large (see Section 4). All of the above detections were accomplished by high-resolution transmission spectroscopy. For HD209458 b, MacDonald & Madhusudhan (2017b) also reported the detection of NH_3 from low-resolution transmission spectroscopy. Giacobbe et al. (2021) detect NH_3 by cross-correlating the observations with synthetic spectra assuming a vertically constant NH_3 abundance of 1.3×10^{-4} , while MacDonald & Madhusudhan (2017b) constrained the NH_3 abundance to 10^{-8} – 2.7×10^{-6} . Our simulations of a Jupiter-mass planet at 1 Gyr yield NH_3 abundances of $\sim 10^{-6}$ at the pressure level of interest for $T_{\text{eq}} = 1400 \text{ K}$ (Figure 2), which appears to be consistent with the constraint by MacDonald & Madhusudhan (2017b). However, we need a more careful analysis for planet specific comparisons, as the eddy diffusion coefficient K_{zz} and intrinsic temperature T_{int} could differ from planet to planet. This is beyond the scope of this study. Since the quenched NH_3 abundance is sensitive to the intrinsic temperature, the potential detection of NH_3 may provide observational tests on the suggested hot deep interiors of hot Jupiters (Thorngren et al. 2019; Fortney et al. 2020).

While we have predicted that warm exoplanets are favorable targets for searching for NH_3 , no previous studies with low-resolution spectroscopy have reported the detection of NH_3 for warm exoplanets. This could be due to the prevalence of clouds and hazes in warm exoplanetary atmospheres that mute the absorption features of gaseous molecules (e.g., Kreidberg et al. 2014, 2018, 2020; Knutson et al. 2014; Wakeford et al. 2017; Chachan et al. 2019, 2020; Libby-Roberts et al. 2020; Mikal-Evans et al. 2021; Alam et al. 2022, see Dymont et al. 2021 for a recent compilation). Since cloud and haze opacity tends to decrease with increasing wavelength, future observations at longer wavelengths would have better chances to detect NH_3 , such as through the detection of $11 \mu\text{m}$ feature. Another possible

³ <https://archive.stsci.edu/prepds/muscles/>

Table 2. Summary of the impacts of planetary properties on NH₃ and HCN abundance and their detectability.

Planetary parameters	Consequence
NH₃	
System age	Young (say $\lesssim 1$ Gyr) age leads to the quenched NH ₃ abundance being lower than bulk N abundance. The effect on feature strengths is moderate owing to compensation between NH ₃ depletion and large scale height.
Planetary mass	High mass (say $\gtrsim 1M_J$) leads to a quenched NH ₃ abundance lower than the bulk N abundance. High mass results in weak NH ₃ features in transmission spectra owing to NH ₃ depletion and small scale height.
Equilibrium temperature	The quenched NH ₃ abundance is insensitive to the equilibrium temperature at $T_{\text{eq}} < 1000$ K. The NH ₃ tends to be depleted by thermochemical conversion to N ₂ at $T_{\text{eq}} \gtrsim 1000$ K. The NH ₃ features in both transmission and emission spectra are relatively strong at $T_{\text{eq}} \sim 400\text{--}1000$ K.
Atmospheric metallicity	High metallicity (say $\gtrsim 10\times$ solar) leads to the quenched NH ₃ abundance being lower than the bulk N abundance. The quenched NH ₃ abundance only weakly depends on metallicity owing to the conversion of additional N to N ₂ . High metallicity weakens NH ₃ features in both transmission and emission spectra.
Eddy diffusion	The quenched NH ₃ abundance is insensitive to K_{zz} . Weak eddy diffusion causes the depletion of NH ₃ owing to thermochemical conversion and photodissociation.
Stellar spectral type	Cool stars with weak NUV flux mitigate the photodissociation of NH ₃ .
HCN	
System age	HCN abundance in the upper atmosphere is nearly the same as the quenched abundance of NH ₃ at deeper layers. Young age reduces HCN abundance due to the depletion of NH ₃ .
Planetary mass	High mass reduces the HCN abundance due to the depletion of NH ₃ .
Equilibrium temperature	The HCN abundance follows the trend of quenched NH ₃ , except for high T_{eq} where CH ₄ is significantly depleted.
Atmospheric metallicity	High metallicity significantly depletes HCN owing to the depletion of CH ₄ .
Eddy diffusion	Strong eddy diffusion lowers the pressure level of HCN formation. HCN features get maximized at intermediate value ($K_{zz} = 10^8 \text{ cm}^2 \text{ s}^{-1}$ in our case) of K_{zz} .
Stellar spectral type	Cool stars with weak NUV flux lowers the pressure level of HCN formation.
Observational suggestions	
Wavelength	Transmission spectra show NH ₃ features of ~ 50 ppm at 1.5, 2, and 11 μm for Jupiter-mass planets around Sun-like stars. Emission spectra show NH ₃ features at 6 and 11 μm for the same conditions. The latter could be > 300 ppm. HCN leaves strong features only at 14 μm in both transmission and emission spectra for solar composition.
Temperature range	Planets with $T_{\text{eq}} \sim 400\text{--}1000$ K would be suitable for detecting NH ₃ .
Strategy	Emission spectrum searching for 11 μm NH ₃ feature is suitable for Jupiter-mass planets with small scale height. Transmission spectrum might be able to find 1.5 and 2 μm features for Saturn-mass planets with large scale height. HCN detection may indicate atmosphere significantly deviated from solar composition, such as high C/O ratio.

cause of the nondetection of NH₃ could be deep atmospheres being much hotter than those predicted by thermal evolution models for non-synchronized exoplanets. For example, [Benneke et al. \(2019\)](#) reported the nondetection of NH₃ on warm sub-Neptune GJ3470b, while the planet is known to have a non-zero eccentricity of $e \sim 0.1$ ([Kosiarek et al. 2019](#)). Such non-zero eccentricity may yield hot deep atmospheres through tidal heating and affect upper atmospheric compositions ([Agúndez et al. 2014b](#); [Fortney et al. 2020](#)).

One of the interesting possibilities for the lack of NH₃ detection is that many warm exoplanets may have atmospheric compositions considerably different from solar composition. For example, if warm exoplanets typically have high metallicity atmospheres, the detection of NH₃ becomes more challenging, as shown in Section 4. The prevalence of high-

metallicity atmospheres may be compatible with the mass-metallicity relation of warm Jupiters ([Thorngren et al. 2016](#)), planet formation models (e.g., [Fortney et al. 2013](#); [Venturini et al. 2016](#); [Cridland et al. 2020](#)), and several atmospheric observations of giant exoplanets ([Wakeford et al. 2018](#); [Carone et al. 2021](#); [JWST Transiting Exoplanet Community Early Release Science Team et al. 2022](#); [Feinstein et al. 2022](#); [Ahrer et al. 2022](#); [Alderson et al. 2022](#); [Rustamkulov et al. 2022](#); [Tsai et al. 2022](#); [Bean et al. 2023](#)). A planet may also have a subsolar N/O ratio if the solid accretion inside the N₂ snowline determines the atmospheric composition (see e.g., Figure 1 of [Paper I](#)), which would also lower the NH₃ abundance as compared that for solar N/O with the same atmospheric metallicity.

5.4. Vertical Variation of Eddy Diffusion Coefficient

While we have assumed vertically constant K_{zz} so far, in reality, the eddy diffusion coefficient likely has a vertical variation (e.g., Zhang & Showman 2018a). The vertically-varying K_{zz} potentially affects our results at some points; for example, it may promote thermochemical conversion of NH_3 to N_2 at deep atmosphere because of low K_{zz} , as seen in Moses et al. (2021). We can test the effect of vertically variable K_{zz} by assuming $K_{zz} = K_{zz,1 \text{ bar}}(P/1 \text{ bar})^{-0.5}$. Following Moses et al. (2021), we also set $K_{zz} = 10^{10} \text{ cm}^2 \text{ s}^{-1}$ at $P > 100 \text{ bar}$ and the maximum value of $K_{zz} = 10^{11} \text{ cm}^2 \text{ s}^{-1}$. Figure 13 shows the photochemical calculation results for various values of $K_{zz,1 \text{ bar}}$. The vertical variable K_{zz} tends to facilitate the thermochemical conversion of NH_3 to N_2 owing to the weak vertical mixing in the deep atmosphere, while it mitigates the NH_3 photodissociation thanks to the strong mixing in the upper atmosphere. The HCN abundance in the upper atmosphere reflects the quenched NH_3 abundance as in the constant K_{zz} case, while HCN abundance at lower atmosphere could be higher compared to constant K_{zz} cases because downward diffusive transport becomes slower as the pressure increases. The vertical variation of K_{zz} and its strength have remained poorly constrained by observations (Kawashima & Min 2021). Future observations of disequilibrium species more sensitive to the quench point than NH_3 is, such as CO, would help to probe K_{zz} in deep atmospheres (e.g., Miles et al. 2020; Mukherjee et al. 2022b).

5.5. Effects of Day-Night Temperature Contrast

Our study has relied on a 1D framework, whereas real exoplanetary atmospheres are in 3D and may show strong temperature contrasts between daysides and nightsides (e.g., Perez-Becker & Showman 2013; Komacek & Showman 2016); however, we do not anticipate that this is a major drawback in this case. Several studies have investigated how horizontal temperature variations and horizontal winds affect the chemistry of exoplanetary atmospheres. These include 3D GCMs (Cooper & Showman 2006; Mendonça et al. 2018; Drummond et al. 2018b,a, 2020), equatorial 2D models (Tsai et al. 2021a), and pseudo-2D models that rotate a 1D model along the equator (Agúndez et al. 2012, 2014a; Moses et al. 2021; Baeyens et al. 2021, 2022). According to the pseudo-2D works by Moses et al. (2021) and Baeyens et al. (2022), the NH_3 abundance is almost invariant with longitudes at warm exoplanets with $T_{\text{eq}} \lesssim 1000 \text{ K}$, except for the pressure level of $\lesssim 10^{-3}$ – 10^{-4} bar where the photodissociation takes place. Drummond et al. (2020) performed 3D global circulation simulations on hot Jupiters HD 189733b and HD 209458b using a 3D GCM that implements a full kinetic chemistry based on a reduced chemical network of Venot et al. (2019) and showed that NH_3 abundance is vertically and longitudinally uniform in both planets, though they

did not include photochemistry. These longitudinal independence could be attributed to the long thermochemical conversion timescale of NH_3 , $> 10^{15} \text{ s}$ at 1000 K (see Figure 4 of Tsai et al. 2018), that is much longer than typical horizontal transport timescales. In the deep atmosphere where the chemical quenching takes place, on the other hand, the atmospheric P – T profile is invariant with longitude because of the long radiative timescale. Thus, we anticipate that the NH_3 spatial distribution in real atmospheres is reasonably approximated by the 1D framework, especially for warm exoplanets that are optimum for detecting NH_3 .

5.6. Observability of N_2 molecule

In Paper I and this study, we have focused on NH_3 and HCN since N_2 , the remaining main N reservoir, in general has negligibly low opacity in visible and infrared wavelengths. However, N_2 actually has moderate opacity at extremely hot temperature, say $> 4000 \text{ K}$. High resolution spectroscopy might still have a chance to detect N_2 if it abundantly exists in hot thermosphere. In the context of terrestrial exoplanets with N_2 dominated atmospheres, Schwieterman et al. (2015) suggested that N_2 can be detected from the absorption feature of $(\text{N}_2)_2$ dimer produced by N_2 – N_2 collisions, though it unlikely affects the observable spectra of giant planets with much lower N_2 abundances. N_2 – H_2 collision-induced absorption (CIA) opacity might still have some impacts; however, quantitative assessment is difficult as of yet owing to the limited valid range of wavelength and temperature for the available CIA absorption coefficient (Karman et al. 2019).

6. SUMMARY

In this study, we have performed a series of photochemical calculations for various values of planetary mass, age, equilibrium temperature, eddy diffusion coefficient, and atmospheric composition to explore the relation between observable NH_3 abundance and bulk nitrogen abundance. Based on the photochemical calculations and the semi-analytic model of NH_3 quenching developed by Paper I (Equation 1), we have comprehensively revealed what planetary properties act to deplete observable NH_3 as compared to bulk nitrogen. Table 2 summarizes how observable abundance of NH_3 and HCN depend on various planetary properties and its observational implications. Our key findings are summarized as follows:

1. As shown in Paper I, the vertically quenched NH_3 abundance is nearly identical to the bulk nitrogen abundance *only* when a planet has a sub-Jupiter mass ($\lesssim 1 \text{ M}_J$) and old age ($\gtrsim 1 \text{ Gyr}$) under the assumption of a solar composition atmosphere.

2. High metallicity atmospheres lead to the quenched NH_3 abundance being much lower than the bulk nitrogen abundance even at sub-Jupiter planet masses and old ages. This highlights the importance of constraining overall atmospheric metallicity for inferring bulk nitrogen abundances.
3. The semi-analytical model of Paper I (Equation 1) reproduces the vertically quenched NH_3 abundance computed by a photochemical kinetic model (Section 2). Thus, our semi-analytical model would mitigate the discrepancy between the quenched NH_3 and bulk nitrogen abundances when inferring the bulk nitrogen abundance from an observed NH_3 .
4. NH_3 is vulnerable to photodissociation and tends to be depleted at 10^{-3} – 10^{-4} bar in clear atmospheres, depending on the equilibrium temperature and eddy diffusion coefficient. The relatively deep pressure level of NH_3 photodissociation is caused by UV photons at 200–230 nm that can penetrate to higher pressures owing to the lack of absorption opacity of other molecules at those wavelengths.
5. The photodissociation of NH_3 is mitigated when planets orbit around cool K and M stars because of the decreased level of NUV photons. Thus, warm planets around K and M stars would be ideal targets for searching for NH_3 .
6. We have examined the NH_3 and HCN signatures in transmission spectra of warm gas giants. For 1 Gyr Jupiter-mass planets with clear atmospheres around Sun-like stars, we have predicted that NH_3 would leave characteristic features of > 50 nm at 1.5, 2.1, and 11 μm in transmission spectrum for the equilibrium temperature of $T_{\text{eq}} \sim 400$ – 1000 K.
7. The emission spectra shows NH_3 features at ~ 6 and 11 μm . For Jupiter-mass planets around Sun-like stars, we have predicted that the 11 μm feature could be > 300 ppm, much larger than that expected for transmission spectra.
8. The 11 μm feature is particularly strong and would be the best signature to identify NH_3 , as clouds and/or hazes tend to have less opacity at such long wavelengths.
9. Our analysis has suggested that it may be difficult to detect HCN by low-resolution spectroscopy if a planet has a solar composition atmosphere. This is because HCN is formed by photochemistry that takes place in the upper atmosphere far away from the pressure level typically probed by observations. The detection

of HCN potentially indicate that atmospheric composition is considerably different from solar composition, such as a high C/O ratio of $\text{C/O} \gg 1$.

Our studies have highlighted that it is not trivial to robustly constrain the atmospheric nitrogen abundances of exoplanets. The observable NH_3 abundance underestimates the bulk nitrogen abundance in most cases. Thus, the observable NH_3 abundance is usually a lower limit of bulk nitrogen abundance, and chemical models are necessary to constrain the bulk nitrogen abundance. This task will be aided by photochemical kinetic models (e.g., Line et al. 2011; Moses et al. 2011; Venot et al. 2013; Kawashima & Ikoma 2018; Molaverdikhani et al. 2019; Tsai et al. 2021b; Hu 2021) and/or retrieval models including disequilibrium chemistry effects (Kawashima & Min 2021; Al-Refaie et al. 2022). Our semi-analytic model (Equation 1) can provide a first estimate on the bulk nitrogen abundance from a retrieved NH_3 abundance.

Although the robust constraint of nitrogen abundance is not easy, we expect that a lower-limit nitrogen abundance still provides some insights on planet formation. For example, for a superstellar N/O ratio, a lower-limit N/O ratio may be able to give a lower-limit orbital distance of planet formation location because gas-phase N/O monotonically increases with the distance (Piso et al. 2016). Alternatively, if planetesimals and/or pebble accretion mainly determine the atmospheric composition, which could be inferred from refractory element abundances in the atmosphere, such as sulfur and alkali metals (e.g., Schneider & Bitsch 2021b; Turini et al. 2021; Hands & Helled 2022; Pacetti et al. 2022), an N/O ratio higher than $\sim 0.1 \times$ stellar value may indicate the planet formation at extremely cold region where N_2 ice could be frozen, as suggested for Jupiter in our Solar System (Owen et al. 1999; Öberg & Wordsworth 2019; Bosman et al. 2019; Ohno & Ueda 2021). Given the unprecedented precision and wavelength coverage of JWST (JWST Transiting Exoplanet Community Early Release Science Team et al. 2022; Feinstein et al. 2022; Ahler et al. 2022; Alderson et al. 2022; Rustamkulov et al. 2022), it will be important to continue to assess what we can learn about planet formation from various elemental ratios of exoplanetary atmospheres.

ACKNOWLEDGEMENTS

We are grateful to anonymous reviewer for insightful comments that greatly improved the quality of this paper. We thank Shang-Min Tsai for helpful instructions on the analysis of VULCAN. We also thank Neel Patel, Masahiro Ikoma, Xinting Yu, Ben Lew, Eliza Kempton, Yuichi Ito, Yui Kawashima, Shota Notsu, Tatsuya Yoshida, and Akifumi Nakayama for fruitful discussions. This work benefited from the 2022 Exoplanet Summer Program in the Other Worlds Laboratory (OWL) at the University of California,

Santa Cruz, a program funded by the Heising-Simons Foundation. Most of numerical computations were carried out on PC cluster at Center for Computational Astrophysics, Na-

tional Astronomical Observatory of Japan. K.O. was supported by JSPS Overseas Research Fellowship. J.J.F. is supported by an award from the Simons Foundation.

REFERENCES

- Adams, D., Gao, P., de Pater, I., & Morley, C. V. 2019, *ApJ*, 874, 61, doi: [10.3847/1538-4357/ab074c](https://doi.org/10.3847/1538-4357/ab074c)
- Agüichine, A., Mousis, O., & Lunine, J. 2022, arXiv e-prints, arXiv:2204.14102. <https://arxiv.org/abs/2204.14102>
- Agúndez, M., Parmentier, V., Venot, O., Hersant, F., & Selsis, F. 2014a, *A&A*, 564, A73, doi: [10.1051/0004-6361/201322895](https://doi.org/10.1051/0004-6361/201322895)
- Agúndez, M., Venot, O., Iro, N., et al. 2012, *A&A*, 548, A73, doi: [10.1051/0004-6361/201220365](https://doi.org/10.1051/0004-6361/201220365)
- Agúndez, M., Venot, O., Selsis, F., & Iro, N. 2014b, *ApJ*, 781, 68, doi: [10.1088/0004-637X/781/2/68](https://doi.org/10.1088/0004-637X/781/2/68)
- Ahrer, E.-M., Stevenson, K. B., Mansfield, M., et al. 2022, arXiv e-prints, arXiv:2211.10489. <https://arxiv.org/abs/2211.10489>
- Al-Refaie, A. F., Venot, O., Changeat, Q., & Edwards, B. 2022, arXiv e-prints, arXiv:2209.11203. <https://arxiv.org/abs/2209.11203>
- Alam, M. K., Kirk, J., Dressing, C. D., et al. 2022, *ApJL*, 927, L5, doi: [10.3847/2041-8213/ac559d](https://doi.org/10.3847/2041-8213/ac559d)
- Alderson, L., Wakeford, H. R., Alam, M. K., et al. 2022, arXiv e-prints, arXiv:2211.10488. <https://arxiv.org/abs/2211.10488>
- Ali-Dib, M. 2017, *MNRAS*, 464, 4282, doi: [10.1093/mnras/stw2651](https://doi.org/10.1093/mnras/stw2651)
- Ali-Dib, M., Mousis, O., Petit, J.-M., & Lunine, J. I. 2014, *ApJ*, 785, 125, doi: [10.1088/0004-637X/785/2/125](https://doi.org/10.1088/0004-637X/785/2/125)
- Arfaux, A., & Lavvas, P. 2022, *MNRAS*, doi: [10.1093/mnras/stac1772](https://doi.org/10.1093/mnras/stac1772)
- Asplund, M., Amarsi, A. M., & Grevesse, N. 2021, *A&A*, 653, A141, doi: [10.1051/0004-6361/202140445](https://doi.org/10.1051/0004-6361/202140445)
- Baeyens, R., Decin, L., Carone, L., et al. 2021, *MNRAS*, 505, 5603, doi: [10.1093/mnras/stab1310](https://doi.org/10.1093/mnras/stab1310)
- Baeyens, R., Konings, T., Venot, O., Carone, L., & Decin, L. 2022, *MNRAS*, 512, 4877, doi: [10.1093/mnras/stac809](https://doi.org/10.1093/mnras/stac809)
- Batalha, N. E., Mandell, A., Pontoppidan, K., et al. 2017, *PASP*, 129, 064501, doi: [10.1088/1538-3873/aa65b0](https://doi.org/10.1088/1538-3873/aa65b0)
- Bean, J. L., Xue, Q., August, P. C., et al. 2023, *Nature*, 618, 43, doi: [10.1038/s41586-023-05984-y](https://doi.org/10.1038/s41586-023-05984-y)
- Benneke, B., Knutson, H. A., Lothringer, J., et al. 2019, *Nature Astronomy*, 3, 813, doi: [10.1038/s41550-019-0800-5](https://doi.org/10.1038/s41550-019-0800-5)
- Bitsch, B., Schneider, A. D., & Kreidberg, L. 2022, arXiv e-prints, arXiv:2207.06077. <https://arxiv.org/abs/2207.06077>
- Booth, R. A., Clarke, C. J., Madhusudhan, N., & Ilee, J. D. 2017, *MNRAS*, 469, 3994, doi: [10.1093/mnras/stx1103](https://doi.org/10.1093/mnras/stx1103)
- Booth, R. A., & Ilee, J. D. 2019, *MNRAS*, 487, 3998, doi: [10.1093/mnras/stz1488](https://doi.org/10.1093/mnras/stz1488)
- Bosman, A. D., Cridland, A. J., & Miguel, Y. 2019, *A&A*, 632, L11, doi: [10.1051/0004-6361/201936827](https://doi.org/10.1051/0004-6361/201936827)
- Carleo, I., Giacobbe, P., Guilluy, G., et al. 2022, arXiv e-prints, arXiv:2207.09761. <https://arxiv.org/abs/2207.09761>
- Carone, L., Mollière, P., Zhou, Y., et al. 2021, *A&A*, 646, A168, doi: [10.1051/0004-6361/202038620](https://doi.org/10.1051/0004-6361/202038620)
- Chachan, Y., Knutson, H. A., Gao, P., et al. 2019, *AJ*, 158, 244, doi: [10.3847/1538-3881/ab4e9a](https://doi.org/10.3847/1538-3881/ab4e9a)
- Chachan, Y., Jontof-Hutter, D., Knutson, H. A., et al. 2020, *AJ*, 160, 201, doi: [10.3847/1538-3881/abb23a](https://doi.org/10.3847/1538-3881/abb23a)
- Charnay, B., Meadows, V., & Leconte, J. 2015, *ApJ*, 813, 15, doi: [10.1088/0004-637X/813/1/15](https://doi.org/10.1088/0004-637X/813/1/15)
- Christie, D. A., Mayne, N. J., Gillard, R. M., et al. 2022, *MNRAS*, 517, 1407, doi: [10.1093/mnras/stac2763](https://doi.org/10.1093/mnras/stac2763)
- Cloutier, R., Charbonneau, D., Deming, D., Bonfils, X., & Astudillo-Defru, N. 2021, *AJ*, 162, 174, doi: [10.3847/1538-3881/ac1584](https://doi.org/10.3847/1538-3881/ac1584)
- Cooper, C. S., & Showman, A. P. 2006, *ApJ*, 649, 1048, doi: [10.1086/506312](https://doi.org/10.1086/506312)
- Cridland, A. J., Pudritz, R. E., & Alessi, M. 2016, *MNRAS*, 461, 3274, doi: [10.1093/mnras/stw1511](https://doi.org/10.1093/mnras/stw1511)
- Cridland, A. J., Pudritz, R. E., Birnstiel, T., Cleeves, L. I., & Bergin, E. A. 2017, *MNRAS*, 469, 3910, doi: [10.1093/mnras/stx1069](https://doi.org/10.1093/mnras/stx1069)
- Cridland, A. J., van Dishoeck, E. F., Alessi, M., & Pudritz, R. E. 2019, *A&A*, 632, A63, doi: [10.1051/0004-6361/201936105](https://doi.org/10.1051/0004-6361/201936105)
- , 2020, *A&A*, 642, A229, doi: [10.1051/0004-6361/202038767](https://doi.org/10.1051/0004-6361/202038767)
- Crossfield, I. J. M., & Kreidberg, L. 2017, *AJ*, 154, 261, doi: [10.3847/1538-3881/aa9279](https://doi.org/10.3847/1538-3881/aa9279)
- Drummond, B., Carter, A. L., Hébrard, E., et al. 2019, *MNRAS*, 486, 1123, doi: [10.1093/mnras/stz909](https://doi.org/10.1093/mnras/stz909)
- Drummond, B., Mayne, N. J., Manners, J., et al. 2018a, *ApJ*, 869, 28, doi: [10.3847/1538-4357/aaeb28](https://doi.org/10.3847/1538-4357/aaeb28)
- , 2018b, *ApJL*, 855, L31, doi: [10.3847/2041-8213/aab209](https://doi.org/10.3847/2041-8213/aab209)
- Drummond, B., Hébrard, E., Mayne, N. J., et al. 2020, *A&A*, 636, A68, doi: [10.1051/0004-6361/201937153](https://doi.org/10.1051/0004-6361/201937153)
- Dymont, A. H., Yu, X., Ohno, K., et al. 2021, arXiv e-prints, arXiv:2112.06173. <https://arxiv.org/abs/2112.06173>
- Eistrup, C. 2022, arXiv e-prints, arXiv:2210.16921. <https://arxiv.org/abs/2210.16921>
- Eistrup, C., Cleeves, L. I., & Krijt, S. 2022, arXiv e-prints, arXiv:2207.13158. <https://arxiv.org/abs/2207.13158>
- Eistrup, C., Walsh, C., & van Dishoeck, E. F. 2016, *A&A*, 595, A83, doi: [10.1051/0004-6361/201628509](https://doi.org/10.1051/0004-6361/201628509)

- . 2018, *A&A*, 613, A14, doi: [10.1051/0004-6361/201731302](https://doi.org/10.1051/0004-6361/201731302)
- Espinoza, N., Fortney, J. J., Miguel, Y., Thorngren, D., & Murray-Clay, R. 2017, *ApJL*, 838, L9, doi: [10.3847/2041-8213/aa65ca](https://doi.org/10.3847/2041-8213/aa65ca)
- Feinstein, A. D., Radica, M., Welbanks, L., et al. 2022, arXiv e-prints, arXiv:2211.10493. <https://arxiv.org/abs/2211.10493>
- Fortney, J. J. 2005, *MNRAS*, 364, 649, doi: [10.1111/j.1365-2966.2005.09587.x](https://doi.org/10.1111/j.1365-2966.2005.09587.x)
- Fortney, J. J., Lodders, K., Marley, M. S., & Freedman, R. S. 2008, *ApJ*, 678, 1419, doi: [10.1086/528370](https://doi.org/10.1086/528370)
- Fortney, J. J., Marley, M. S., & Barnes, J. W. 2007, *ApJ*, 659, 1661, doi: [10.1086/512120](https://doi.org/10.1086/512120)
- Fortney, J. J., Marley, M. S., Lodders, K., Saumon, D., & Freedman, R. 2005, *ApJL*, 627, L69, doi: [10.1086/431952](https://doi.org/10.1086/431952)
- Fortney, J. J., Mordasini, C., Nettelmann, N., et al. 2013, *ApJ*, 775, 80, doi: [10.1088/0004-637X/775/1/80](https://doi.org/10.1088/0004-637X/775/1/80)
- Fortney, J. J., Visscher, C., Marley, M. S., et al. 2020, *AJ*, 160, 288, doi: [10.3847/1538-3881/abc5bd](https://doi.org/10.3847/1538-3881/abc5bd)
- France, K., Loyd, R. O. P., Youngblood, A., et al. 2016, *ApJ*, 820, 89, doi: [10.3847/0004-637X/820/2/89](https://doi.org/10.3847/0004-637X/820/2/89)
- Fray, N., & Schmitt, B. 2009, *Planet. Space Sci.*, 57, 2053, doi: [10.1016/j.pss.2009.09.011](https://doi.org/10.1016/j.pss.2009.09.011)
- Gao, P., & Benneke, B. 2018, *ApJ*, 863, 165, doi: [10.3847/1538-4357/aad461](https://doi.org/10.3847/1538-4357/aad461)
- Gao, P., & Zhang, X. 2020, *ApJ*, 890, 93, doi: [10.3847/1538-4357/ab6a9b](https://doi.org/10.3847/1538-4357/ab6a9b)
- Gao, P., Thorngren, D. P., Lee, G. K. H., et al. 2020, *Nature Astronomy*, doi: [10.1038/s41550-020-1114-3](https://doi.org/10.1038/s41550-020-1114-3)
- Gao, P., Piette, A. A. A., Steinrueck, M. E., et al. 2023, arXiv e-prints, arXiv:2305.05697, doi: [10.48550/arXiv.2305.05697](https://doi.org/10.48550/arXiv.2305.05697)
- Gautier, D., Hersant, F., Mousis, O., & Lunine, J. I. 2001, *ApJL*, 550, L227, doi: [10.1086/319648](https://doi.org/10.1086/319648)
- Giacobbe, P., Brogi, M., Gandhi, S., et al. 2021, *Nature*, 592, 205, doi: [10.1038/s41586-021-03381-x](https://doi.org/10.1038/s41586-021-03381-x)
- Greene, T. P., Line, M. R., Montero, C., et al. 2016, *ApJ*, 817, 17, doi: [10.3847/0004-637X/817/1/17](https://doi.org/10.3847/0004-637X/817/1/17)
- Gueymard, C. A. 2018, *Solar Energy*, 169, 434, doi: [10.1016/j.solener.2018.04.067](https://doi.org/10.1016/j.solener.2018.04.067)
- Guillot, T., & Hueso, R. 2006, *MNRAS*, 367, L47, doi: [10.1111/j.1745-3933.2006.00137.x](https://doi.org/10.1111/j.1745-3933.2006.00137.x)
- Guilluy, G., Giacobbe, P., Carleo, I., et al. 2022, arXiv e-prints, arXiv:2207.09760. <https://arxiv.org/abs/2207.09760>
- Hands, T. O., & Helled, R. 2022, *MNRAS*, 509, 894, doi: [10.1093/mnras/stab2967](https://doi.org/10.1093/mnras/stab2967)
- Helling, C., Woitke, P., Rimmer, P. B., et al. 2014, *Life*, 4, 142, doi: [10.3390/life4020142](https://doi.org/10.3390/life4020142)
- Hobbs, R., Shorttle, O., & Madhusudhan, N. 2021, arXiv e-prints, arXiv:2112.04930. <https://arxiv.org/abs/2112.04930>
- Hobbs, R., Shorttle, O., Madhusudhan, N., & Rimmer, P. 2019, *MNRAS*, 487, 2242, doi: [10.1093/mnras/stz1333](https://doi.org/10.1093/mnras/stz1333)
- Hu, R. 2021, *ApJ*, 921, 27, doi: [10.3847/1538-4357/ac1789](https://doi.org/10.3847/1538-4357/ac1789)
- Husser, T. O., Wende-von Berg, S., Dreizler, S., et al. 2013, *A&A*, 553, A6, doi: [10.1051/0004-6361/201219058](https://doi.org/10.1051/0004-6361/201219058)
- JWST Transiting Exoplanet Community Early Release Science Team, Ahrer, E.-M., Alderson, L., Batalha, N. M., et al. 2022, *Nature*
- Karman, T., Gordon, I. E., van der Avoird, A., et al. 2019, *Icarus*, 328, 160, doi: [10.1016/j.icarus.2019.02.034](https://doi.org/10.1016/j.icarus.2019.02.034)
- Kawashima, Y., & Ikoma, M. 2018, *ApJ*, 853, 7, doi: [10.3847/1538-4357/aaa0c5](https://doi.org/10.3847/1538-4357/aaa0c5)
- . 2019, *ApJ*, 877, 109, doi: [10.3847/1538-4357/ab1b1d](https://doi.org/10.3847/1538-4357/ab1b1d)
- Kawashima, Y., & Min, M. 2021, *A&A*, 656, A90, doi: [10.1051/0004-6361/202141548](https://doi.org/10.1051/0004-6361/202141548)
- Kempton, E. M. R., Zhang, M., Bean, J. L., et al. 2023, arXiv e-prints, arXiv:2305.06240, doi: [10.48550/arXiv.2305.06240](https://doi.org/10.48550/arXiv.2305.06240)
- Knutson, H. A., Benneke, B., Deming, D., & Homeier, D. 2014, *Nature*, 505, 66, doi: [10.1038/nature12887](https://doi.org/10.1038/nature12887)
- Komacek, T. D., & Showman, A. P. 2016, *ApJ*, 821, 16, doi: [10.3847/0004-637X/821/1/16](https://doi.org/10.3847/0004-637X/821/1/16)
- Komacek, T. D., Showman, A. P., & Parmentier, V. 2019, *ApJ*, 881, 152, doi: [10.3847/1538-4357/ab338b](https://doi.org/10.3847/1538-4357/ab338b)
- Kosiarek, M. R., Crossfield, I. J. M., Hardegree-Ullman, K. K., et al. 2019, *AJ*, 157, 97, doi: [10.3847/1538-3881/aaf79c](https://doi.org/10.3847/1538-3881/aaf79c)
- Kreidberg, L. 2018, in *Handbook of Exoplanets*, ed. H. J. Deeg & J. A. Belmonte, 100, doi: [10.1007/978-3-319-55333-7_100](https://doi.org/10.1007/978-3-319-55333-7_100)
- Kreidberg, L., Line, M. R., Thorngren, D., Morley, C. V., & Stevenson, K. B. 2018, *ApJL*, 858, L6, doi: [10.3847/2041-8213/aabfce](https://doi.org/10.3847/2041-8213/aabfce)
- Kreidberg, L., Bean, J. L., Désert, J.-M., et al. 2014, *Nature*, 505, 69, doi: [10.1038/nature12888](https://doi.org/10.1038/nature12888)
- Kreidberg, L., Mollière, P., Crossfield, I. J. M., et al. 2020, arXiv e-prints, arXiv:2006.07444. <https://arxiv.org/abs/2006.07444>
- Lavvas, P., & Arfaux, A. 2021, *MNRAS*, 502, 5643, doi: [10.1093/mnras/stab456](https://doi.org/10.1093/mnras/stab456)
- Lavvas, P., & Koskinen, T. 2017, *ApJ*, 847, 32, doi: [10.3847/1538-4357/aa88ce](https://doi.org/10.3847/1538-4357/aa88ce)
- Lavvas, P., Koskinen, T., Steinrueck, M. E., García Muñoz, A., & Showman, A. P. 2019, *ApJ*, 878, 118, doi: [10.3847/1538-4357/ab204e](https://doi.org/10.3847/1538-4357/ab204e)
- Libby-Roberts, J. E., Berta-Thompson, Z. K., Désert, J.-M., et al. 2020, *AJ*, 159, 57, doi: [10.3847/1538-3881/ab5d36](https://doi.org/10.3847/1538-3881/ab5d36)
- Line, M. R., Vasisht, G., Chen, P., Angerhausen, D., & Yung, Y. L. 2011, *ApJ*, 738, 32, doi: [10.1088/0004-637X/738/1/32](https://doi.org/10.1088/0004-637X/738/1/32)
- Line, M. R., Wolf, A. S., Zhang, X., et al. 2013, *ApJ*, 775, 137, doi: [10.1088/0004-637X/775/2/137](https://doi.org/10.1088/0004-637X/775/2/137)
- Lodders, K., & Fegley, B. 2002, *Icarus*, 155, 393, doi: [10.1006/icar.2001.6740](https://doi.org/10.1006/icar.2001.6740)
- Loyd, R. O. P., France, K., Youngblood, A., et al. 2016, *ApJ*, 824, 102, doi: [10.3847/0004-637X/824/2/102](https://doi.org/10.3847/0004-637X/824/2/102)

- MacDonald, R. J., & Madhusudhan, N. 2017a, *ApJL*, 850, L15, doi: [10.3847/2041-8213/aa97d4](https://doi.org/10.3847/2041-8213/aa97d4)
- . 2017b, *MNRAS*, 469, 1979, doi: [10.1093/mnras/stx804](https://doi.org/10.1093/mnras/stx804)
- Madhusudhan, N., Amin, M. A., & Kennedy, G. M. 2014, *ApJL*, 794, L12, doi: [10.1088/2041-8205/794/1/L12](https://doi.org/10.1088/2041-8205/794/1/L12)
- Madhusudhan, N., Bitsch, B., Johansen, A., & Eriksson, L. 2017, *MNRAS*, 469, 4102, doi: [10.1093/mnras/stx1139](https://doi.org/10.1093/mnras/stx1139)
- Marley, M. S., & McKay, C. P. 1999, *Icarus*, 138, 268, doi: [10.1006/icar.1998.6071](https://doi.org/10.1006/icar.1998.6071)
- Marley, M. S., & Robinson, T. D. 2015, *ARA&A*, 53, 279, doi: [10.1146/annurev-astro-082214-122522](https://doi.org/10.1146/annurev-astro-082214-122522)
- McKay, C. P., Pollack, J. B., & Courtin, R. 1989, *Icarus*, 80, 23, doi: [10.1016/0019-1035\(89\)90160-7](https://doi.org/10.1016/0019-1035(89)90160-7)
- Mendonça, J. M., Tsai, S.-m., Malik, M., Grimm, S. L., & Heng, K. 2018, *ApJ*, 869, 107, doi: [10.3847/1538-4357/aaed23](https://doi.org/10.3847/1538-4357/aaed23)
- Menou, K. 2019, *MNRAS*, 485, L98, doi: [10.1093/mnras/512/1/98](https://doi.org/10.1093/mnras/512/1/98)
- . 2021, arXiv e-prints, arXiv:2112.12127. <https://arxiv.org/abs/2112.12127>
- Mikal-Evans, T., Crossfield, I. J. M., Benneke, B., et al. 2021, *AJ*, 161, 18, doi: [10.3847/1538-3881/abc874](https://doi.org/10.3847/1538-3881/abc874)
- Miles, B. E., Skemer, A. J. I., Morley, C. V., et al. 2020, *AJ*, 160, 63, doi: [10.3847/1538-3881/ab9114](https://doi.org/10.3847/1538-3881/ab9114)
- Miller-Ricci Kempton, E., Zahnle, K., & Fortney, J. J. 2012, *ApJ*, 745, 3, doi: [10.1088/0004-637X/745/1/3](https://doi.org/10.1088/0004-637X/745/1/3)
- Molaverdikhani, K., Henning, T., & Mollière, P. 2019, *ApJ*, 883, 194, doi: [10.3847/1538-4357/ab3e30](https://doi.org/10.3847/1538-4357/ab3e30)
- . 2020, *ApJ*, 899, 53, doi: [10.3847/1538-4357/aba52b](https://doi.org/10.3847/1538-4357/aba52b)
- Mollière, P., van Boekel, R., Dullemond, C., Henning, T., & Mordasini, C. 2015, *ApJ*, 813, 47, doi: [10.1088/0004-637X/813/1/47](https://doi.org/10.1088/0004-637X/813/1/47)
- Mollière, P., Molyarova, T., Bitsch, B., et al. 2022, arXiv e-prints, arXiv:2204.13714. <https://arxiv.org/abs/2204.13714>
- Monga, N., & Desch, S. 2015, *ApJ*, 798, 9, doi: [10.1088/0004-637X/798/1/9](https://doi.org/10.1088/0004-637X/798/1/9)
- Morley, C. V., Fortney, J. J., Kempton, E. M.-R., et al. 2013, *ApJ*, 775, 33, doi: [10.1088/0004-637X/775/1/33](https://doi.org/10.1088/0004-637X/775/1/33)
- Morley, C. V., Fortney, J. J., Marley, M. S., et al. 2012, *ApJ*, 756, 172, doi: [10.1088/0004-637X/756/2/172](https://doi.org/10.1088/0004-637X/756/2/172)
- . 2015, *ApJ*, 815, 110, doi: [10.1088/0004-637X/815/2/110](https://doi.org/10.1088/0004-637X/815/2/110)
- Morley, C. V., Knutson, H., Line, M., et al. 2017, *AJ*, 153, 86, doi: [10.3847/1538-3881/153/2/86](https://doi.org/10.3847/1538-3881/153/2/86)
- Moses, J. I., Madhusudhan, N., Visscher, C., & Freedman, R. S. 2013a, *ApJ*, 763, 25, doi: [10.1088/0004-637X/763/1/25](https://doi.org/10.1088/0004-637X/763/1/25)
- Moses, J. I., Tremblin, P., Venot, O., & Miguel, Y. 2021, *Experimental Astronomy*, doi: [10.1007/s10686-021-09749-1](https://doi.org/10.1007/s10686-021-09749-1)
- Moses, J. I., Visscher, C., Keane, T. C., & Sperier, A. 2010, *Faraday Discussions*, 147, 103, doi: [10.1039/c003954c](https://doi.org/10.1039/c003954c)
- Moses, J. I., Visscher, C., Fortney, J. J., et al. 2011, *ApJ*, 737, 15, doi: [10.1088/0004-637X/737/1/15](https://doi.org/10.1088/0004-637X/737/1/15)
- Moses, J. I., Line, M. R., Visscher, C., et al. 2013b, *ApJ*, 777, 34, doi: [10.1088/0004-637X/777/1/34](https://doi.org/10.1088/0004-637X/777/1/34)
- Mousis, O., Ronnet, T., & Lunine, J. I. 2019, *ApJ*, 875, 9, doi: [10.3847/1538-4357/ab0a72](https://doi.org/10.3847/1538-4357/ab0a72)
- Mukherjee, S., Batalha, N. E., Fortney, J. J., & Marley, M. S. 2022a, arXiv e-prints, arXiv:2208.07836. <https://arxiv.org/abs/2208.07836>
- Mukherjee, S., Fortney, J. J., Batalha, N. E., et al. 2022b, *ApJ*, 938, 107, doi: [10.3847/1538-4357/ac8dfb](https://doi.org/10.3847/1538-4357/ac8dfb)
- Notsu, S., Ohno, K., Ueda, T., et al. 2022, *ApJ*, 936, 188, doi: [10.3847/1538-4357/ac87fa](https://doi.org/10.3847/1538-4357/ac87fa)
- Öberg, K. I., & Bergin, E. A. 2016, *ApJL*, 831, L19, doi: [10.3847/2041-8205/831/2/L19](https://doi.org/10.3847/2041-8205/831/2/L19)
- Öberg, K. I., Murray-Clay, R., & Bergin, E. A. 2011, *ApJL*, 743, L16, doi: [10.1088/2041-8205/743/1/L16](https://doi.org/10.1088/2041-8205/743/1/L16)
- Öberg, K. I., & Wordsworth, R. 2019, *AJ*, 158, 194, doi: [10.3847/1538-3881/ab46a8](https://doi.org/10.3847/1538-3881/ab46a8)
- Ohno, K., & Fortney, J. J. 2023, *ApJ*, 946, 18, doi: [10.3847/1538-4357/acafed](https://doi.org/10.3847/1538-4357/acafed)
- Ohno, K., & Kawashima, Y. 2020, *ApJL*, 895, L47, doi: [10.3847/2041-8213/ab93d7](https://doi.org/10.3847/2041-8213/ab93d7)
- Ohno, K., & Okuzumi, S. 2018, *ApJ*, 859, 34, doi: [10.3847/1538-4357/aabee3](https://doi.org/10.3847/1538-4357/aabee3)
- Ohno, K., Okuzumi, S., & Tazaki, R. 2020, *ApJ*, 891, 131, doi: [10.3847/1538-4357/ab44bd](https://doi.org/10.3847/1538-4357/ab44bd)
- Ohno, K., & Tanaka, Y. A. 2021, *ApJ*, 920, 124, doi: [10.3847/1538-4357/ac1516](https://doi.org/10.3847/1538-4357/ac1516)
- Ohno, K., & Ueda, T. 2021, *A&A*, 651, L2, doi: [10.1051/0004-6361/202141169](https://doi.org/10.1051/0004-6361/202141169)
- Owen, T., Mahaffy, P., Niemann, H. B., et al. 1999, *Nature*, 402, 269, doi: [10.1038/46232](https://doi.org/10.1038/46232)
- Pacetti, E., Turrini, D., Schisano, E., et al. 2022, arXiv e-prints, arXiv:2206.14685. <https://arxiv.org/abs/2206.14685>
- Parmentier, V., Showman, A. P., & Lian, Y. 2013, *A&A*, 558, A91, doi: [10.1051/0004-6361/201321132](https://doi.org/10.1051/0004-6361/201321132)
- Pelletier, S., Benneke, B., Darveau-Bernier, A., et al. 2021, *AJ*, 162, 73, doi: [10.3847/1538-3881/ac0428](https://doi.org/10.3847/1538-3881/ac0428)
- Perez-Becker, D., & Showman, A. P. 2013, *ApJ*, 776, 134, doi: [10.1088/0004-637X/776/2/134](https://doi.org/10.1088/0004-637X/776/2/134)
- Pinhas, A., Madhusudhan, N., Gandhi, S., & MacDonald, R. 2019, *MNRAS*, 482, 1485, doi: [10.1093/mnras/sty2544](https://doi.org/10.1093/mnras/sty2544)
- Piso, A.-M. A., Öberg, K. I., Birnstiel, T., & Murray-Clay, R. A. 2015, *ApJ*, 815, 109, doi: [10.1088/0004-637X/815/2/109](https://doi.org/10.1088/0004-637X/815/2/109)
- Piso, A.-M. A., Pegues, J., & Öberg, K. I. 2016, *ApJ*, 833, 203, doi: [10.3847/1538-4357/833/2/203](https://doi.org/10.3847/1538-4357/833/2/203)
- Rustamkulov, Z., Sing, D. K., Mukherjee, S., et al. 2022, arXiv e-prints, arXiv:2211.10487. <https://arxiv.org/abs/2211.10487>
- Sagan, C., & Chyba, C. 1997, *Science*, 276, 1217, doi: [10.1126/science.276.5316.1217](https://doi.org/10.1126/science.276.5316.1217)

- Saumon, D., Marley, M. S., Cushing, M. C., et al. 2006, *ApJ*, 647, 552, doi: [10.1086/505419](https://doi.org/10.1086/505419)
- Schneider, A. D., & Bitsch, B. 2021a, *A&A*, 654, A71, doi: [10.1051/0004-6361/202039640](https://doi.org/10.1051/0004-6361/202039640)
- . 2021b, *A&A*, 654, A72, doi: [10.1051/0004-6361/202141096](https://doi.org/10.1051/0004-6361/202141096)
- Schwieterman, E. W., Robinson, T. D., Meadows, V. S., Misra, A., & Domagal-Goldman, S. 2015, *ApJ*, 810, 57, doi: [10.1088/0004-637X/810/1/57](https://doi.org/10.1088/0004-637X/810/1/57)
- Stassun, K. G., Oelkers, R. J., Paegert, M., et al. 2019, *AJ*, 158, 138, doi: [10.3847/1538-3881/ab3467](https://doi.org/10.3847/1538-3881/ab3467)
- Steinrueck, M. E., Koskinen, T., Lavvas, P., et al. 2023, arXiv e-prints, arXiv:2305.09654, doi: [10.48550/arXiv.2305.09654](https://doi.org/10.48550/arXiv.2305.09654)
- Steinrueck, M. E., Showman, A. P., Lavvas, P., et al. 2021, *MNRAS*, 504, 2783, doi: [10.1093/mnras/stab1053](https://doi.org/10.1093/mnras/stab1053)
- Tan, X. 2022, *MNRAS*, 511, 4861, doi: [10.1093/mnras/stac344](https://doi.org/10.1093/mnras/stac344)
- Thiabaud, A., Marboeuf, U., Alibert, Y., Leya, I., & Mezger, K. 2015, *A&A*, 574, A138, doi: [10.1051/0004-6361/201424868](https://doi.org/10.1051/0004-6361/201424868)
- Thorngren, D., Gao, P., & Fortney, J. J. 2019, *ApJL*, 884, L6, doi: [10.3847/2041-8213/ab43d0](https://doi.org/10.3847/2041-8213/ab43d0)
- Thorngren, D. P., Fortney, J. J., Murray-Clay, R. A., & Lopez, E. D. 2016, *ApJ*, 831, 64, doi: [10.3847/0004-637X/831/1/64](https://doi.org/10.3847/0004-637X/831/1/64)
- Tsai, S.-M., Innes, H., Lichtenberg, T., et al. 2021a, *ApJL*, 922, L27, doi: [10.3847/2041-8213/ac399a](https://doi.org/10.3847/2041-8213/ac399a)
- Tsai, S.-M., Kitzmann, D., Lyons, J. R., et al. 2018, *ApJ*, 862, 31, doi: [10.3847/1538-4357/aac834](https://doi.org/10.3847/1538-4357/aac834)
- Tsai, S.-M., Lyons, J. R., Grosheintz, L., et al. 2017, *ApJS*, 228, 20, doi: [10.3847/1538-4365/228/2/20](https://doi.org/10.3847/1538-4365/228/2/20)
- Tsai, S.-M., Malik, M., Kitzmann, D., et al. 2021b, *ApJ*, 923, 264, doi: [10.3847/1538-4357/ac29bc](https://doi.org/10.3847/1538-4357/ac29bc)
- Tsai, S.-M., Lee, E. K. H., Powell, D., et al. 2022, arXiv e-prints, arXiv:2211.10490. <https://arxiv.org/abs/2211.10490>
- Turrini, D., Schisano, E., Fonte, S., et al. 2021, *ApJ*, 909, 40, doi: [10.3847/1538-4357/abd6e5](https://doi.org/10.3847/1538-4357/abd6e5)
- Venot, O., Bounaceur, R., Dobrijevic, M., et al. 2019, *A&A*, 624, A58, doi: [10.1051/0004-6361/201834861](https://doi.org/10.1051/0004-6361/201834861)
- Venot, O., Hébrard, E., Agúndez, M., et al. 2013, in *Astrophysics and Space Science Proceedings*, Vol. 35, The Early Evolution of the Atmospheres of Terrestrial Planets, ed. J. M. Trigo-Rodríguez, F. Raulin, C. Müller, & C. Nixon, 67, doi: [K18-74538](https://doi.org/10.1007/978-94-007-7453-8_4)
- Venturini, J., Alibert, Y., & Benz, W. 2016, *A&A*, 596, A90, doi: [10.1051/0004-6361/201628828](https://doi.org/10.1051/0004-6361/201628828)
- Wakeford, H. R., Sing, D. K., Kataria, T., et al. 2017, *Science*, 356, 628, doi: [10.1126/science.aah4668](https://doi.org/10.1126/science.aah4668)
- Wakeford, H. R., Sing, D. K., Deming, D., et al. 2018, *AJ*, 155, 29, doi: [10.3847/1538-3881/aa9e4e](https://doi.org/10.3847/1538-3881/aa9e4e)
- Welbanks, L., Madhusudhan, N., Allard, N. F., et al. 2019, *ApJL*, 887, L20, doi: [10.3847/2041-8213/ab5a89](https://doi.org/10.3847/2041-8213/ab5a89)
- Wolf, E. T., & Toon, O. B. 2010, *Science*, 328, 1266, doi: [10.1126/science.1183260](https://doi.org/10.1126/science.1183260)
- Youngblood, A., France, K., Loyd, R. O. P., et al. 2016, *ApJ*, 824, 101, doi: [10.3847/0004-637X/824/2/101](https://doi.org/10.3847/0004-637X/824/2/101)
- Zahnle, K. J., & Marley, M. S. 2014, *ApJ*, 797, 41, doi: [10.1088/0004-637X/797/1/41](https://doi.org/10.1088/0004-637X/797/1/41)
- Zhang, X., & Showman, A. P. 2018a, *ApJ*, 866, 1, doi: [10.3847/1538-4357/aada85](https://doi.org/10.3847/1538-4357/aada85)
- . 2018b, *ApJ*, 866, 2, doi: [10.3847/1538-4357/aada7c](https://doi.org/10.3847/1538-4357/aada7c)